

# Lawrence Berkeley National Laboratory

## Recent Work

### Title

AN ANALYSIS OF  $K-p \rightarrow n^+n^-$  IN THE REGION OF THE  $A(1520)$

### Permalink

<https://escholarship.org/uc/item/7xn0j17c>

### Authors

Mast, Terry S.  
Alston-Garnjost, Margaret.  
Bangerter, Roger O.  
et al.

### Publication Date

1971-08-01

Submitted to Nuclear Physics  
also a Ph. D. Thesis

RECEIVED  
LAWRENCE  
RADIATION LABORATORY

LBL-301  
Preprint *c. 2*



TWO-WEEK LOAN COPY

This is a Library Circulating Copy  
which may be borrowed for two weeks.  
For a personal retention copy, call  
Tech. Info. Division, Ext. 5545

LIBRARY AND  
DOCUMENTS SECTION

AN ANALYSIS OF  $K^-_p \rightarrow \Lambda \pi^+ \pi^-$  IN THE REGION  
OF THE  $\Lambda(1520)$

Terry S. Mast, Margaret Alston-Garnjost, Roger O. Bangerter,  
Angela Barbaro-Galtieri, Frank T. Solmitz, and  
Robert D. Tripp

August 1971



AEC Contract No. W-7405-eng-48

*4 a*

## **DISCLAIMER**

This document was prepared as an account of work sponsored by the United States Government. While this document is believed to contain correct information, neither the United States Government nor any agency thereof, nor the Regents of the University of California, nor any of their employees, makes any warranty, express or implied, or assumes any legal responsibility for the accuracy, completeness, or usefulness of any information, apparatus, product, or process disclosed, or represents that its use would not infringe privately owned rights. Reference herein to any specific commercial product, process, or service by its trade name, trademark, manufacturer, or otherwise, does not necessarily constitute or imply its endorsement, recommendation, or favoring by the United States Government or any agency thereof, or the Regents of the University of California. The views and opinions of authors expressed herein do not necessarily state or reflect those of the United States Government or any agency thereof or the Regents of the University of California.

AN ANALYSIS OF  $K^- p \rightarrow \Lambda \pi^+ \pi^-$  IN THE REGION OF THE  $\Lambda(1520)$ 

Terry S. Mast, Margaret Alston-Garnjost, Roger O. Bangerter,  
Angela Barbaro-Galtieri, Frank T. Solnitz, and Robert D. Tripp

Lawrence Berkeley Laboratory, University of California  
Berkeley, California 94720

## ABSTRACT

The rate for the decay  $\Lambda(1520) \rightarrow \Sigma(1385) \pi$  has been measured in a study of the reaction sequence  $K^- p \rightarrow \Lambda(1520) \rightarrow \Sigma(1385) \pi \rightarrow \Lambda \pi^+ \pi^-$ . A sample of 9200 events of the type  $K^- p \rightarrow \Lambda \pi^+ \pi^-$  has been obtained in the Berkeley 25-inch hydrogen bubble chamber. The incident momenta range from 300 to 470 MeV/c. After correction for detection efficiency, an energy-independent partial-wave analysis was performed using an isobar model. The model included a coherent mixture of six partial waves to describe all mass distributions, angular distributions, and the polarization of the lambda. The  $\Sigma(1385) \pi$  decay mode was found to dominate the  $\Lambda \pi^+ \pi^-$  decay of the  $\Lambda(1520)$ , in disagreement with the results of a production reaction study of the same decay. The width for the decay was measured to be  $1.66 \pm .25$  MeV. Mixing between the  $\Lambda(1520)$  and the  $\Lambda(1690)$  has been used in the past to describe the  $J^P = 3/2^-$  baryons as SU(3) singlet and octet. Combining our rate for  $\Lambda(1520)$  with a recently measured rate for  $\Lambda(1690) \rightarrow \Sigma(1385) \pi$ , we calculate the mixing angle  $|\theta| = 65$  to  $85$  deg. This is in strong disagreement with the mixing angle derived from the two-body D-wave decays of the singlet and octet of  $-25 \pm 6$  deg. Thus, some modification of the usual SU(3) description of these states needs to be made.

## I. INTRODUCTION

Within the framework of SU(3), the known  $J^P = 3/2^-$  baryons have been treated as a singlet and octet by several authors.<sup>1,2</sup> The rates for the D-wave decays of the octet disagree with the predictions of SU(3), and the masses of the octet members fail to satisfy the Gell-Mann Okubo mass relation. These discrepancies have been successfully removed by invoking configuration mixing between the primarily singlet state  $\Lambda(1520)$  and the primarily octet state  $\Lambda(1690)$ . Data now are becoming available on the S-wave decays of these states into members of the  $3/2^+$  decuplet and the  $0^-$  meson octet.<sup>3-6</sup> These provide a further test of the SU(3) nature of these baryons. For example, if the  $\Lambda(1520)$  were a pure SU(3) singlet, then its decay through an SU(3)-invariant process to  $\Sigma(1385)\pi$  would be forbidden. Consistent with the mixed nature of the  $\Lambda(1520)$ , however, this decay is observed. The rate for the decay was measured in a production experiment,<sup>5</sup> and the mixing angle calculated from that rate was consistent with the angle derived from the mass relation and the D-wave decays.<sup>1,2</sup>

In this experiment, we study the decay in the formation reaction  $K^-p \rightarrow \Lambda(1520) \rightarrow \Sigma(1385)\pi$ .<sup>24</sup> An increase in the number of events by a factor of 100 from the experiment which discovered the  $\Lambda(1520)$  allows a very detailed analysis.<sup>7</sup> In section II we describe the experimental procedures, the bias corrections applied to the data, and the overall features of the data. The Dalitz plot is dominated by  $\Sigma(1385)$  production. The angular distribution of the lambda indicates dominance of  $J^P = 3/2^-$  formation. In order to extract the modes and rates for the decay of  $\Lambda(1520)$  from the data, we have performed a

partial-wave analysis of the three-particle final state using an isobar model. This analysis is described in Section III and yields information about the formation process as well as the decay modes of  $\Lambda(1520)$ . The rate into  $\Sigma(1385)\pi$  disagrees with the result from the production experiment measurement by more than a factor of two. In Section IV, the result from our experiment is combined with other data on the  $3/2^-$  baryons to yield a new mixing angle. This value for the mixing angle strongly disagrees with the value derived from the two-body D-wave decays. Appendix A describes in detail the investigation made of detection efficiencies and the weighting applied to correct for losses. Appendix B gives the detailed formulae used in the isobar model.

## II. EXPERIMENTAL PROCEDURES

The  $K^-$  beam for this experiment was designed and built by Drs. Joseph Murray and Roger Bangerter, and was operated in conjunction with the Berkeley 25-inch hydrogen bubble chamber. The beam has been fully described elsewhere.<sup>8</sup> The beam design successfully overcame the two major difficulties of a low-momentum  $K^-$  beam: the high background-to- $K^-$  ratio at the target (about 1000:1) and the decay loss of  $K^-$  in the beam (about 10% per foot at 400 MeV/c). In an unseparated beam, the background-to- $K^-$  ratio would increase to about 50 000:1 in the 40 feet from target to bubble chamber. Two-stage conventional separation might reduce this ratio to 10:1. A new electrostatic septum filter was developed for this experiment and obtained a background-to- $K^-$  ratio at the bubble chamber of about 1:5. The filter operates by passing the beam between stacks

of closely spaced high-voltage electrodes which deflect background particles into uranium bars located between the stacks. It has a transmission of about 25% and in less than 7 feet achieves a rejection of the order of  $10^5$ .

During the period August 1965 to July 1967, an exposure of  $1.3 \times 10^6$  pictures was obtained. Typically each picture contained 6  $K^-$  tracks and 2 background tracks. The background consisted of pions, muons, and some electrons. Background tracks had close to minimum ionization and were thus easily distinguished from the  $K^-$  tracks, which has 2.6 times minimum ionization.

By movement of the target and by use of a beryllium beam degrader, we were able to obtain  $K^-$  momenta between 270 and 470 MeV/c. The data were taken with 20 different beam settings. However, most of the pathlength (Fig. 1) occurs close to 395 MeV/c, the momentum required to form the  $\Lambda(1520)$ .

The film was scanned for all topologies including those with a lambda vee and two charged pions in the final state. All of the film was scanned once; 38% was scanned twice; and 7% was scanned three times. All events within a restricted fiducial volume were measured with the Spiral Reader or Franckenstein measuring projectors. The kinematic reconstruction and the fit to reaction hypotheses were performed with the programs TVGP and SQUAW. Events which failed to fit a reaction hypothesis were remeasured until 94% of the total sample of the lambda-two-pion events passed. The remaining failing events were unmeasurable due to the obscuration of a track or the presence of a very short track.

A sample of tau decays of the beam was measured and fitted in

order to determine the beam characteristics for each of the 20 beam settings. The mean momentum, the rms spread of the momentum, and a momentum position correlation were established for each setting. The mean momentum from the tau decays was averaged with the measured momentum for each of the lambda-two-pion events prior to the fitting to a reaction hypothesis. The magnetic field in the chamber was 18.7 kG, and the beam tracks were typically measured with an uncertainty of 8 to 12 MeV/c. After beam averaging and fitting to  $K^- p \rightarrow \Lambda \pi^+ \pi^-$ , the final sample of events had a mean uncertainty of 3.6 MeV/c and the distribution shown in Fig. 2.

Only those events which fit a reaction hypothesis with a confidence level greater than 0.01 were accepted for further analysis; 14800 such events satisfied the 7-constraint fit to  $K^- p \rightarrow \Lambda \pi^+ \pi^-$  and 336 events passed the 5-constraint fit to  $K^- p \rightarrow \Sigma^0 \pi^+ \pi^-$ . Ten ambiguous events fit both hypotheses. Reinspection showed them to be mis-measured and they were eliminated from the sample.

To insure sufficient tracklength for a good measurement of the lambda momentum, further restrictions were made on the fiducial volumes for the production and decay vertices. These reduced the sample to 10296 events. To correct for a scanning loss of short-length lambdas, all events with a projected length less than 2.5 mm were eliminated and the remaining 9412 events were weighted to account for the cut. The weighting also accounted for loss due to escape from the decay vertex fiducial volume. The mean weight was 1.18. Further losses were investigated by looking at the distribution of the decay proton in the lambda rest frame. Anisotropy in this distribution was found coming from the loss of events with

short-length protons and events with the lambda vee seen edge on by the scanners. These biases were removed by rejecting events with a proton length less than 3 mm and weighting the remaining events. This reduced the sample to 9227 events with a mean weight of 1.21. A detailed description of the analysis and application of these cuts and weights is given in Appendix A.

The lifetime distribution of the final sample is shown in Fig. 3. In order to remove the effect of the cut on short-length lambdas, the events have been plotted as a function of  $(t-t_0)$  in units of the known lambda lifetime. For each event,  $t_0$  is given by  $2.5 \text{ mm}/\eta c\tau_\Lambda \cos \lambda$  where  $\eta$  is the ratio of the lambda momentum to its mass and  $\lambda$  is the dip angle. The distribution is consistent with the line corresponding to the known lifetime ( $\tau_\Lambda = 2.51 \times 10^{-10}$  sec.).

The cross section for the reaction was determined from a path-length based on the tau decays of the beam. The analysis of these taus has been described in a previous publication.<sup>9</sup> The numbers of both taus and  $\Lambda\pi\pi$  events were corrected for unobserved decay modes and for scanning efficiencies.

The scanning efficiencies were determined from the multiple scans using an extension of the method developed by Derenzo and Hildebrand.<sup>10</sup> The analysis accounts for the differing visibility of events by parametrizing a visibility function  $f(v)$ ;  $f(v)$  is the fraction of the sample seen with an efficiency  $v$ , where  $v$  varies from 0.0 to 1.0. The extension used for this experiment defines a different visibility ( $v_1$ ,  $v_2$ , and  $v_3$ ) for each of the three scans. The events found on each of the scans are fitted to determine the parameters of the function  $f(v_1, v_2, v_3)$ , which is then used to calculate the

efficiencies. Details of this analysis can be found in Ref. 11. The overall scanning efficiency was 0.96.

The beam-averaging procedure described above averaged the measured momentum for each event with the central momentum of the distribution. For events with large uncertainty in the measured beam momentum, this procedure artificially reduced the width of the beam distribution. This then led to different cross sections for different beam settings. It can be shown that true beam distribution is restored by spreading out the contribution of each event with a Gaussian with width equal to the fitted momentum uncertainty. This was done for both the taus and  $\Lambda\pi^+\pi^-$  events. In the region of high statistics, this made changes in the cross section of the order of 10%. This procedure successfully removed the disagreements between the cross sections calculated from different beam settings.

### III. SEMIQUANTITATIVE DESCRIPTION OF THE DATA

The momentum dependence of the partial cross section for  $K^-p \rightarrow \Lambda\pi^+\pi^-$  is shown in Fig. 4 and listed in Table I. The  $\Lambda(1520)$  dominates the cross section in the region near 400 MeV/c, and a substantial background exists beyond this region. The two data points represented by circles are results from an experiment at higher energies.<sup>12</sup> A quantitative separation of resonance and background contributions is given by the partial-wave analysis described in the following section.

Dalitz plots as a function of incident momentum are shown in Fig. 5. The Dalitz plot is roughly uniformly populated below 360 MeV/c

and above 420 MeV/c. Between 380 and 410 MeV/c, bands of increased density at high  $\Lambda\pi$  invariant mass correspond to  $\Sigma(1385)$  production. The center of the  $\Sigma(1385)$  band occurs at an invariant mass squared of  $1.92 \text{ (GeV)}^2$ , which is outside the kinematically allowed region for all but the highest momenta. The  $\Sigma(1385)$  bands are accompanied by an enhancement in the low  $\pi\pi$  mass region. This enhancement is generated by the constructive interference of the  $\Sigma(1385)^+$  and  $\Sigma(1385)^-$ . The presence of the  $\Sigma(1385)$  bands and the enhancement of low  $\pi\pi$  masses can also be seen in the Dalitz plot projections (Figs. 6, 7, and 8).

The constructive interference between  $\Sigma(1385)^+$  and  $\Sigma(1385)^-$  indicates the dominance of symmetric ( $I = 0$ ) production. Additional evidence for the dominance of the  $I = 0$  amplitude comes from some preliminary results on the reaction  $K^-p \rightarrow \Lambda\pi^0\pi^0$ . An analysis is in progress of the zero-prong plus lambda topology from the same exposure. In order to separate the contributions from  $\Lambda\pi^0$ ,  $\Sigma\pi^0$ , and  $\Lambda\pi^0\pi^0$  final states, a fit has been made to the angular distribution and polarization of the lambda as a function of the mass of the missing neutrals. Preliminary results indicate a cross section for  $K^-p \rightarrow \Lambda\pi^0\pi^0$  which is about half the  $\Lambda\pi^+\pi^-$  cross section at all incident momenta. This ratio is expected from pure  $I = 0$  production, so the  $I = 1$  contribution to the  $\Lambda\pi^+\pi^-$  cross section must be small.

A more sensitive measure of the amount of  $I = 1$  production is given by the charge asymmetry of the Dalitz plot, shown as a function of incident momentum in Fig. 9. The asymmetry is defined as

$$\alpha = \frac{N^- - N^+}{N^- + N^+}, \quad (1)$$

where  $N^-$  is the number of events with a  $\Lambda\pi^-$  invariant mass larger than a  $\Lambda\pi^+$  invariant mass. This asymmetry can be generated by two effects. A mass difference between  $\Sigma(1385)^-$  and  $\Sigma(1385)^+$  introduces an asymmetry even when the amplitudes for their production are equal. In addition, the asymmetry can arise from the interference between  $I = 0$  and  $I = 1$  production. In the case of  $\Sigma(1385)$  production, this corresponds to unequal production of  $\Sigma(1385)^-$  and  $\Sigma(1385)^+$ . If the masses of the  $\Sigma(1385)^-$  and  $\Sigma(1385)^+$  were equal, the asymmetry would be related to the isospin production amplitudes as follows:

$$\alpha = \frac{2\text{Re} \int M_0^* M_1 d\rho}{\int |M_0 + M_1|^2 d\rho}. \quad (2)$$

An  $I = 1$  amplitude ( $M_1$ ) about 10% as large as the  $I = 0$  amplitude ( $M_0$ ) is sufficient to explain the observed structure. Thus the  $I = 1$  contribution to the partial cross section is of the order of a few per cent.

The production angular distribution of the lambda with respect to the incident beam is shown as a function of incident momentum in Fig. 10. The distribution changes dramatically with momentum. It is forward peaked at 360 MeV/c, approaches a  $(1 + 3 \cos^2\theta)$  distribution near 395 MeV/c, and becomes backward peaked at 430 MeV/c. A  $(1 + 3 \cos^2\theta)$  distribution is expected from a pure  $J^P = 3/2$  state decaying into  $3/2^+$  and  $0^-$  states. These angular distributions and the polarization of the lambda have been fitted to a Legendre polynomial expansion using a maximum-likelihood technique. The probability for each event was described by



$$1 + \sum_{\ell=1}^4 \frac{A_{\ell}}{A_0} P_{\ell}(\cos \theta) + \alpha_{\Lambda} \cos \beta \sum_{\ell=1}^4 \frac{B_{\ell}}{A_0} P'_{\ell}(\cos \theta). \quad (3)$$

Here  $\cos \theta = \hat{K} \cdot \hat{\Lambda}$  and  $\cos \beta = \frac{\hat{K} \times \hat{\Lambda}}{|\hat{K} \times \hat{\Lambda}|} \cdot \hat{p}$ , where  $\hat{K}$ ,  $\hat{\Lambda}$ , and  $\hat{p}$  are unit vectors in the direction of the  $K^-$ ,  $\Lambda$ , and decay-proton momenta. The  $K^-$  and  $\Lambda$  momenta are defined in the overall c.m. frame, and the decay proton is defined in the  $\Lambda$  rest frame. The weak decay asymmetry  $\alpha_{\Lambda}$  was set equal to 0.645. The  $A_{\ell}/A_0$  and  $B_{\ell}/B_0$  coefficients resulting from the fit are plotted as a function of incident momentum in Fig. 11. The polynomial fits are shown as curves over the data in Fig. 10. The dramatic changes in the angular distributions are reflected in the structure in  $A_1/A_0$  and  $A_2/A_0$ . This rapid variation and the presence of polarization indicate interference between states of different parity. A quantitative and simultaneous description of these angular distributions and the mass distributions is given by the isobar-model partial-wave analysis.

#### IV. PARTIAL-WAVE ANALYSIS

In order to separate the background from the  $\Lambda(1520)$  production and to determine the modes of the  $\Lambda(1520)$  decay, we have fit the data to an isobar model. The model treats the three-particle final state as the production of a particle and an isobar followed by the decay of the isobar, shown schematically in Fig. 12. The notation is defined in Table II. Four types of "isobars" have been chosen for this analysis:

- (1) A  $\Lambda$  and  $\pi$  resonating as  $\Sigma(1385)$ , denoted by " $Y^*$ ."
- (2) A  $\Lambda$  and  $\pi$  in a relative S-wave, denoted by " $\Lambda\pi$ ."
- (3) The two pions in a relative S-wave, denoted by " $\sigma$ ."
- (4) The two pions in a relative P-wave, denoted by " $\rho$ ."

The incident and isobar-production waves chosen for this analysis are shown in Table III. Since the energy available in the final state is so low, only S and P waves have been used.

There are many formulations of the isobar model; Morgan gives a nice summary of the assumptions involved and a full list of references.<sup>13</sup> For the most part we have followed the practical formulation of Deler and Valladas.<sup>14</sup> The amplitude for the process indicated in Fig. 12, where particles 2 ( $\pi^+$ ) and 3 ( $\Lambda$ ) form the isobar, is written as a product of an energy-dependent factor and a factor describing the spin and angular-momentum decomposition:

$$A_{23}^{K \mu_f \mu_i} = T_{23}^K(E, m_{23}) f_{23}^{K \mu_f \mu_i}(\Omega_i, \Omega_f, \omega_{23}), \quad (4)$$

where  $K$  represents the quantum numbers  $J$ ,  $L$ ,  $L'$ ,  $j$ , and  $\ell$ , and takes on the values corresponding to the waves of Table III. The indices  $\mu_f$  and  $\mu_i$  refer to the incident proton and final lambda spin projections onto the axis of quantization.  $E$  is the center-of-mass energy, and  $m_{23}$  is the invariant mass of particles 2 and 3.

The energy-dependent factor accounts for angular-momentum barriers and final-state interactions of particles 2 and 3. The precise form that this factor should take is not well understood, and we have primarily followed the prescriptions used by Morgan in an analysis of

$N\pi\pi$ .<sup>13</sup> The detailed energy dependence used for each of the four types of waves is described in Appendix B.

For the second factor, describing the spin and angular decomposition, we have followed the formulation of Deler and Valladas; the explicit formulae are described in Appendix B.

The amplitudes for the  $Y^*$  and  $\Lambda\pi$  waves have been combined to form isospin-0 and isospin-1 amplitudes:

$$\begin{aligned} A_0^{K\mu_f\mu_i} &= \frac{1}{\sqrt{3}} (A_{23}^{K\mu_f\mu_i} + A_{13}^{K\mu_f\mu_i}), \\ A_1^{K\mu_f\mu_i} &= \frac{1}{\sqrt{2}} (A_{23}^{K\mu_f\mu_i} - A_{13}^{K\mu_f\mu_i}). \end{aligned} \quad (5)$$

Similar isospin combinations were made for the  $\pi\pi$  waves.

The isospin amplitudes were normalized such that

$$\sum_{\mu_f\mu_i} \int |A_I^{K\mu_f\mu_i}|^2 dp = 4\pi\lambda^2 (J + 1/2), \quad (6)$$

where the integral is over the three-body phase space.

The decay of the lambda contains polarization information; this has been incorporated by constructing new amplitudes,  $M_I^{K\mu_p\mu_i}$ , which are linear combinations of the above A's.  $\mu_p$  is the spin projection of the lambda-decay proton; and  $\theta$  and  $\psi$  describe the orientation of the decay proton.

$$\begin{aligned} M_I^{K\frac{1}{2}\mu_i} &= A_I^{K(-\frac{1}{2})\mu_i} [-P \sin\theta e^{-i\psi}] + A_I^{K\frac{1}{2}\mu_i} [S - P \cos\theta], \\ M_I^{K(-\frac{1}{2})\mu_i} &= A_I^{K(-\frac{1}{2})\mu_i} [S + P \cos\theta] + A_I^{K\frac{1}{2}\mu_i} [-P \sin\theta e^{i\psi}]. \end{aligned} \quad (7)$$

S and P are the amplitudes describing the weak decay of the lambda;

they have been set real with a ratio  $S/P = 2.735$  corresponding to an asymmetry of 0.645.<sup>15</sup>

In terms of these amplitudes the probability for each event is given by

$$P(\Omega_i, \Omega_f, \omega_{23}, \omega_\Lambda, E, m_{23}) = \frac{|\sum_K a_{KM_I}^{K\mu_p\mu_i}|^2}{\int \sum_K |a_{KM_I}^{K\mu_p\mu_i}|^2 dp} \quad (8)$$

This probability has been used in an event-by-event likelihood fit to the data.

The data were divided into 9 bins of incident momentum (Table IV) and energy-independent fits were made to the data in each bin. All of the fitting was done with a CDC-6600 using the program OPTIME which varied the real and imaginary parts of  $a_K$ . The set of waves used at all momenta was chosen by preliminary fittings in the region of high statistics, 370 to 400 MeV/c. For these three bins the likelihoods for about 11,000 randomly generated "starting solutions" with all 17 waves of Table III were calculated. The four "starting solutions" with the highest likelihoods at each momentum were then optimized. Those waves with an amplitude less than one standard deviation from zero were rejected and the solution remaximized. Only those solutions where  $Y^*DS03$  dominated gave high likelihoods with a small number of waves and reasonable continuity in momentum. The set of these solutions with the highest likelihoods included 6 waves and these were then used as starting solutions for the next lowest and highest momentum bins. In this way the solution was propagated from momentum to momentum. The amplitudes thus achieved are plotted in

the Argand diagrams of Fig. 13 and listed in Table V. The continuity achieved by the propagation of solutions is reasonable.

Since there is an overall free phase at each momentum, the fits were performed with the amplitude for  $Y^*DS03$  fixed real. In the Argand diagrams, the amplitudes at each momentum have been rotated so the phase ( $\delta$ ) of the  $Y^*DS03$  wave corresponds to the phase of a  $\Lambda(1520)$  Breit-Wigner described below. The overall scale of the amplitudes has been fixed to agree with the measured cross sections of Table I. We emphasize, however, that the relative amount of each wave at each momentum is freely determined by the fit. Thus, in addition to the excellent continuity, there is very good agreement of the  $Y^*DS03$  amplitude with the  $\Lambda(1520)$  Breit-Wigner, shown as a curve in Fig. 13(a).

The total width for the Breit-Wigner form used includes D-wave barriers (with a radius of interaction of 1 fermi) for the  $\bar{K}N$  and  $\Sigma\pi$  partial widths. The partial width for  $\Lambda(1520) \rightarrow \Sigma(1385)\pi$  contains only an effective phase-space factor since the reaction proceeds through a final S-wave. The effective phase space was taken to be the integral of the isobar-model amplitude  $Y^*DS03$ . This is essentially equivalent to averaging the relative momentum of the  $\Sigma(1385)\pi$  system over the P-wave Breit-Wigner shape of the  $\Sigma(1385)$ . The good agreement with the energy-independent points in Fig. 13(a) confirms the momentum dependence of the  $\Lambda(1520)$  Breit-Wigner form.

The  $Y^*DS13$  wave is the only wave with isospin = 1. This wave is very small and shows no obvious continuous pattern from momentum to momentum. The  $Y^*PP01$  amplitude contributes significantly and tends to grow with momentum. The  $Y^*PP03$  is small and shows no continuous behavior. The  $\sigma PS01$  is the major background wave

and remains approximately fixed. This wave, with all particles in a relative S-wave, represents the usual "phase space" background contribution. Finally the  $\sigma DP03$  amplitude is small. It represents the non- $\Sigma(1385)$  component of the  $D03, \Lambda(1520)$ . Within the errors and uncertainty in the model, this  $\sigma DP03$  amplitude varies roughly as a Breit-Wigner.

The final fit involves no waves of the " $\Lambda\pi$ " or " $\rho$ " types. However, substituting the  $\Lambda\pi PS01$  and  $\Lambda\pi DP03$  for the  $\sigma PS01$  and the  $\sigma DP03$  made essentially no change in the amplitudes and only slightly lowered the likelihood. Thus the data cannot distinguish between the slightly different mass distributions predicted by the two types of waves.

Considering the many assumptions involved in the isobar model, the small waves here probably have little physical significance; more than likely they represent the mismatch between the data and the model. The large waves hopefully are representing the physical behavior of the reaction.

In order to illustrate the agreement between the fit and the data, a set of Monte Carlo events were generated isotropically in phase space and then weighted with the probability of Eq. 8, using the final parameters from the fit. The  $\Lambda\pi$  and  $\pi\pi$  mass distributions thus predicted are shown as curves over the data in Figs. 6, 7, and 8. The fit accurately reproduces the mass distributions at each momentum. The chi-square for each plot is shown in Table VI.

The Dalitz-plot asymmetry from the fit is in good agreement with the data, as shown in Fig. 9. The amount of this asymmetry that comes from the  $\Sigma(1385)^- \Sigma(1385)^+$  mass difference was investigated by generating a set of Monte Carlo events without the  $I = 1$

amplitude  $Y^* DS13$ . The resulting asymmetry was equal to  $-0.06$  and essentially independent of incident momentum in the region of interest.

Finally, the Monte Carlo events were fitted with the probability of Eq. 3 in order to find  $A_\ell$  and  $B_\ell$  and compare them with those from the data. The Monte Carlo results are shown as dots in Fig. 11. The agreement with the major structure in  $A_1/A_0$  and  $A_2/A_0$  is very good. However, there is disagreement with the polarization. Although the fit yielded some  $B_1/A_0$  with the correct sign, it systematically failed to provide enough. In addition, we should emphasize that the B coefficients used for the comparison only describe one component of the lambda polarization. The isobar model describes the whole polarization vector, and the fit uses all the polarization information from the data. However, because of the particular waves involved, the component describe by the B's is expected to be the most important.

Our conclusion from the fitting then is that the  $\Lambda\pi^+\pi^-$  final state of the  $\Lambda(1520)$  is dominated by  $\Sigma(1385)\pi$ . This is made more quantitative by considering the cross sections for the only two waves coming from the  $\Lambda(1520)$  (and the only two D waves), the  $Y^* DS03$  and the  $\sigma DP03$ . The contribution to the cross section of each of these waves is plotted in Fig. 14. Both are seen to peak at 395 MeV/c. The ratio of  $Y^* DS03$  cross section to the sum of  $Y^* DS03$  and  $\sigma DP03$  cross sections is given in Fig. 15. The fraction due to  $Y^* DS03$  remains constant throughout the  $\Lambda(1520)$  region at a value of about 0.97. The final value for the branching fraction

$$(\Lambda(1520) \rightarrow \Sigma(1385)\pi \rightarrow \Lambda\pi\pi) / (\Lambda(1520) \rightarrow \Lambda\pi\pi) \text{ is } 0.97 \begin{matrix} + 0.03 \\ - 0.10 \end{matrix}$$

The error has been estimated on the basis of varying some of the

input parameters to the model and by studying the sensitivity of the branching fraction to the inclusion of different sets of amplitudes consistent with a reasonable energy continuity. Reasonable variations of the masses and widths of the  $\Sigma(1385)$  did not significantly affect the results.

The result for the branching fraction from this experiment disagrees strongly with the result  $0.39 \pm .10$  quoted from the production experiment of Burkhardt et al.<sup>5</sup> The production experiment has many fewer events (206 events) than the present experiment and has the additional problem of extracting the  $\Lambda(1520)$  signal from the  $\Lambda\pi^+\pi^-\pi^0$  final states. They divide the data into three mass intervals centered on the  $\Lambda(1520)$ . The data in the central interval (with about 15% background) agrees with ours and yields a branching fraction consistent with ours. The data in the side intervals (with about 30% background) yield lower branching fractions and contribute to their low overall value.

In order to calculate the partial width, we have assumed the world average values of  $16 \pm 2$  MeV for the  $\Lambda(1520)$  total width and  $9.6 \pm 0.7\%$  for the branching fraction into  $\Lambda\pi\pi$ .<sup>17</sup> Using a branching fraction for  $\Sigma(1385)$  into  $\Lambda\pi$  of  $0.90 \pm 0.03$ , we calculate a width for  $\Lambda(1520) \rightarrow \Sigma(1385)\pi$  of  $1.66 \pm 0.25$  MeV.

## V. SU(3) IMPLICATIONS AND CONCLUSIONS

The information presently known about the  $J^P = 3/2^-$  baryons is listed in Table VII. Previous analyses of these baryons have ordered the first five states listed into a singlet and an octet;<sup>1,2</sup> and with the data known at the time, this treatment was successful. By involving

configuration mixing between the  $\Lambda(1520)$  and  $\Lambda(1690)$ , these analyses were able to derive mixing angles from a) the Gell-Mann Okubo mass relation, b) the D-wave decays into baryon octet and meson octet, and c) the S-wave decays into baryon decuplet and meson octet. The mixing angles derived from these three independent methods were in agreement.

We now reexamine this situation in the light of present experimental knowledge of these baryons and the results of this experiment. The physical  $\Lambda(1520)$  and  $\Lambda(1690)$  states are related to the pure singlet and octet states as follows:

$$\begin{aligned} |(1520)\rangle &= \cos\theta |1\rangle - \sin\theta |8\rangle, \\ |(1690)\rangle &= +\sin\theta |1\rangle + \cos\theta |8\rangle. \end{aligned} \quad (9)$$

The Gell-Mann Okubo mass relation gives the mixing angle in terms of the masses:

$$\cos^2\theta = \frac{m_8 - m_{1520}}{m_{1690} - m_{1520}}, \quad \text{where } m_8 = \frac{1}{3}(2m_N - 2m_{\Xi} - m_{\Sigma}). \quad (10)$$

In fact, this relation is not a very strong constraint on the mixing angle, largely due to the considerable uncertainty in the  $\Xi$  mass. Previous analyses optimistically chose the mass to be  $1819 \pm 6$  MeV and found a mixing angle of  $21 \pm 4$  deg.<sup>1</sup> However, a more conservative choice which reflects the confused experimental situation would be  $m_{\Xi} = 1832 \pm 37$ . The resulting mixing angle is  $|\theta| = (13 \pm 22)$  deg.<sup>18</sup>

The D-wave decays of the singlet and octet have been recently summarized by Plane et al.<sup>2</sup> Using the decay rates into stable baryons and mesons, they perform a fit to derive the F and D coupling

constants and the mixing angle. No information about the  $\Xi$  state was used in the fit. With 5 degrees of freedom they found  $\chi^2 = 0.8$  and a mixing angle  $\theta = -25 \pm 6$  deg.

Data on decays into decuplet plus pion via the S-wave are slowly becoming available.<sup>5,6</sup> Previous analyses were based on rough limits.<sup>1,5</sup> The SU(3) prediction relates the coupling constants and mixing angle, so some assumption must be made to relate the experimentally measured partial widths and the coupling constants. The usual prescription for decay into stable particles is the potential-theory relation, which for S-wave decay is

$$\Gamma = C^2 g^2 p \frac{M_N}{M_R}. \quad (11)$$

Here  $C$  is an SU(3) Clebsch-Gordan coefficient,  $M_R$  and  $M_N$  are the resonance and nucleon masses, and  $p$  is the c.m. momentum of the decay products. The factor  $p/M_R$  represents the phase space available to the decay. For a decay into unstable particles this should be replaced by an integral over the phase space of the matrix element squared.

The following formula has been adopted:

$$\Gamma = C^2 g^2 I, \quad \text{where } I = \int |Y^* DS03|^2 d\rho. \quad (12)$$

The integral  $I$  as a function of incident momentum in the region of the  $\Lambda(1520)$  and the  $\Lambda(1690)$  is shown in Fig. 16. The increased fraction of  $\Sigma(1385)$ , which lies in the physical region as the energy increases, accounts for the rapid increase in  $I$  compared with three body phase space, the curve labeled  $\rho$  in Fig. 16.

The partial widths for the S-wave decays of  $\Lambda(1520)$  and  $\Lambda(1690)$  can be used to determine the mixing angle. Using Eq. 9 and the fact that an SU(3) singlet is forbidden to decay to  $\Sigma(1385)\pi$ , we derive

$$\tan^2 \theta = \frac{\Gamma_{1520}}{\Gamma_{1690}} \frac{I_{1690}}{I_{1520}} \quad (13)$$

Previous estimates for the partial width for  $\Lambda(1690) \rightarrow \Sigma(1385)\pi$  were based on an upper limit of about 10 MeV.<sup>4</sup> However, a recent analysis with increased statistics yields a very small amplitude for the decay, 0.06.<sup>6</sup> Assuming an elasticity of 0.2 and a total width of 55 MeV,<sup>16</sup> this amplitude implies a partial width into  $\Sigma(1385)\pi$  of 1.0 MeV. However, there is an estimated uncertainty of 0.03 on the amplitude.<sup>19</sup> and there is a large uncertainty in the total width of about 30 MeV. These large uncertainties allow values for the partial width from 0.1 to 3.44 MeV.

With  $I_{1690}/I_{1520}$  equal to 9.54<sup>20</sup> and  $\Gamma_{1520}$  equal to 1.66 MeV, we have used Eq. 13 to calculate  $|\theta|$  for these limits on the  $\Gamma_{1690}$  partial width. With  $\Gamma_{1690} = 0.1$  MeV,  $|\theta|$  equals 85 deg; and with  $\Gamma_{1690} = 3.44$  MeV,  $|\theta|$  equals 65 deg. In order to obtain agreement with the mixing angle from the D-wave decays ( $\theta = -25$  deg), the partial width for the  $\Lambda(1690)$  would have to be 73 MeV! In the light of this large discrepancy, the simple singlet-octet description of these decays no longer appears to be valid.

A possible explanation of the discrepancy may be due to a mis-assignment of the currently observed states. More detailed data on all states in this energy region is required to test this hypothesis.

With the abandonment of the simple singlet-octet picture, the situation rapidly becomes complicated. Turning to the quark model,<sup>21</sup>

which has had considerable success in accounting for the baryon states, we find predictions for two  $J^P = 3/2^-$  octets and one  $3/2^-$  decuplet.

However, experimental information on these states is very sketchy.

As indicated in Table VII, possible members of the second octet and the decuplet have been seen. However, the last three states have

masses too high to be plausibly associated with the missing octet and they are usually regarded to arise from radial excitations. In terms of the quark model there can be spin-orbit mixing of the two octets, and in addition there can be mixing of the decuplet with the two octets by SU(3)-breaking forces. On the basis of a specific model for quark interactions, Faiman has estimated the possible mixing between the octets and singlet.<sup>22</sup> Treating the baryon resonances as bound states of three paraquarks interacting via harmonic-oscillator forces, he derives two possible singlet-octet mixing angles for the  $\Lambda(1520)$ ,  $\theta = 63$  deg and  $\theta = 75$  deg. With new data becoming available on the decays of  $3/2^-$  states into decuplets and pions, further constraints will be imposed on possible multiplet members and realistic tests of specific models may become available.

#### ACKNOWLEDGMENTS

We express our appreciation to Dr. Joseph Murray and Roger Gearhart for their valuable contributions to the initial phases of the experiment. We also wish to thank the 25-inch bubble-chamber crew and our scanning and measuring staff for their conscientious assistance. David Herndon, Larry Miller, and especially Werner Koellner provided valuable assistance with the computer programming of the isobar-model fits. We gratefully acknowledge helpful discussion with Dr. Gerard Smadja. It is a pleasure to acknowledge the support of Professor Luis W. Alvarez.

## APPENDICES

A. Investigation of Biases and Weighting

We describe here the analysis of scanning and measuring losses and the weighting used to account for them. The known distributions of four variables were used to investigate event loss: the lambda lifetime, the polar cosine and azimuth of the lambda-decay proton, and the azimuth of the lambda production about the beam.

Each measured event within the production vertex fiducial volume was weighted by  $\exp(t/\tau_\Lambda)$ , where  $t = l/\eta c$ ,  $l$  is the length of the lambda, and  $\eta = p/m$  the ratio of the laboratory momentum to the mass of the lambda. These weighted events are plotted in Fig. 17 as a function of the lambda length projected onto the scanning plane. If the events were distributed as  $\exp(-t/\tau_\Lambda)$ , this distribution would be constant. A loss of short-length lambdas is indicated by the sharp decrease for projected lengths less than 0.25 cm. Above this projected length, the distribution remains constant until loss of lambdas due to escape from the chamber again causes a decrease (not shown in the figure). To account for this short-length loss and the escape loss, all events with a projected length less than 0.25 cm were removed from the sample and the remaining events were weighted by the inverse probability of their detection:

$$\frac{1.0}{\exp(-0.25/\eta c \tau_\Lambda \cos \lambda) - \exp(-l_p/\eta c \tau_\Lambda)} \quad (21)$$

Here  $\lambda$  is the dip angle that the lambda makes with the scanning plane. The potential distance of the lambda  $l_p$  was defined as the distance from the production vertex to the edge of the decay fiducial

volume in the direction of the lambda line of flight.

The distribution of the decay proton should be isotropic in the lambda rest frame. Figure 18 shows a scatter plot of  $\cos\theta$ , the cosine of the angle between the proton and lambda, versus  $p_{\text{lab}}$ , the laboratory momentum of the lambda. The depletion of events at low momentum and near  $\cos\theta = -1.0$  is due to a loss of events with a short-length proton. Events with a proton length less than 3 mm (corresponding to a laboratory momentum of 102 MeV/c) were removed from the sample (Fig. 19). The remaining events were weighted as a function of laboratory momentum according to the fraction of the decay cosine removed.

The distributions of  $\cos\theta$  and  $\psi$ , the azimuth of the decay proton, showed only small additional deviations from isotropy. These occurred when the proton went directly forward from the lambda ( $\cos\theta = 1.0$ ), corresponding to a lambda vee with a  $180^\circ$  opening angle) or when the lambda vee was seen edge on by the scanner. These losses, which occurred for low-momentum lambdas, were analyzed as follows. "Inner" and "outer" volumes were defined in the space of  $\cos\theta$ ,  $\psi$ , and  $p_{\text{lab}}$ . The "outer" volume contained the total populated region after the short-length proton cut. The  $\cos\theta$  boundaries of the "inner" volume are shown in dashed lines on Fig. 19. The  $\psi$  boundary of the "inner" volume excludes those events where the lambda vee is seen edge on by the scanner at  $\psi < 36^\circ$ . These "inner" and "outer" volumes were chosen on the basis of the  $\cos\theta$  and  $\psi$  distributions so that the events in the "inner" volume were isotropic. Detection efficiency of 100% was then assumed for the "inner" volume. The ratio of the numbers of events in the volumes compared with the ratio of the sizes of the volumes was used

to test for losses. A weight correcting for such losses is plotted as a function of  $p_{lab}$  in Fig. 20. There is a small loss for momenta less than 150 MeV/c. The straight line is a "smoothed" decay weight applied to the events.

The final weight applied to each event in the analysis was the product of the lifetime weight, the short-proton weight, and the decay weight.

The azimuthal distribution of the lambda about the beam should be isotropic. Figure 21 shows the events weighted for the previous losses plotted against the lambda azimuth. Azimuths of 0 and  $\pi$  correspond to lambdas moving toward and away from the scanner;  $\pi/2$  corresponds to events moving left and right. The distribution shows no additional losses.

### B. Isobar Model Formulae

In this appendix we define in detail the two factors in the isobar-model amplitudes used in Eq. 4 of the text.

The energy-dependent factor  $T_{23}$  describes the amplitude for an "isobar" formed with particles 2 and 3. In general, it contains an angular-momentum barrier for the production of the isobar and a final-state factor describing the interactions of particles 2 and 3. The latter factor is either a Breit-Wigner form or a Watson final-state factor, depending on the type of wave involved. The following equations define  $T_{23}$  for each of the four types of waves used in the analysis. The variables are defined in Table II and Fig. 12:

$$\text{For "Y*"}, T_{23} = \frac{1}{\sqrt{p_1 p_1'}} \frac{\sqrt{\Gamma}}{m_{23} - m_R + \frac{i\Gamma}{2}} B(p_1, L'), \quad (14)$$

where

$$B(p_1, L') = \left[ \frac{p_1^{2L'+1}}{(1 + p_1^2 R^2)^{L'}} \right]^{1/2}$$

and  $R$ , the radius of interaction, was chosen to be 1 fermi. The resonance parameters chosen for the  $\Sigma(1385)$  were as follows:

$$\begin{aligned} m_R [\Sigma^+(1385)] &= 1.384 \text{ GeV} \\ m_R [\Sigma^-(1385)] &= 1.388 \text{ GeV} \end{aligned} \quad (15)$$

and  $\Gamma = 9.3 (p_1')^3 / (1 + (R p_1')^2)$ , corresponding to a width of 0.040 GeV, at the resonant energy.

$$\text{For "}\Lambda\pi\text{"}, T_{23} = \frac{1}{\sqrt{p_1 p_1'}} \frac{e^{i\delta} \sin \delta}{(p_1')^{\ell+1/2}} B(p_1, L') \quad (16)$$

and  $\delta = 2.88 (m_{23} - 1.255)$ .

This parametrization of the  $\Lambda\pi$  S-wave phase shift has been taken from the K-matrix analysis of low-energy  $\bar{K}N$  scattering by Martin and Sakitt.<sup>23</sup>

$$\text{For "}\sigma\text{"}, T_{12} = \frac{1}{\sqrt{p_3 p_3'}} \frac{e^{i\delta} \sin \delta}{(p_3')^{1/2}} B(p_3, L') \quad (17)$$

and  $p_3' \cot \delta = m_{12} \left( \frac{1}{.32} - 109.5 (p_3')^2 + 1114. (p_3')^4 \right)$

$$\text{For "}\rho\text{"}, T_{12} = \frac{1}{\sqrt{p_3 p_3'}} \frac{e^{i\delta} \sin \delta}{(p_3')^{1/2}} B(p_3, L') \quad (18)$$

and  $(p_3')^3 \cot \delta = \frac{m_{12}}{2} \left[ \frac{1 - 0.1609 (p_3'/m_\pi)^2}{1.375} \right]$ .

The  $I = 0$  parametrization corresponds to a scattering length of  $0.16 m_\pi^{-1}$ .<sup>13</sup> The  $I = 1$  phase shift corresponds to a resonance



of mass equal to 0.750 GeV and width equal to 0.100 GeV.<sup>13</sup>

The formulae for the spin and angular-momentum dependence are the same as those derived by Deler and Valladas. We quote here an especially simple formulation. The angles and spin are defined in Table II and Figs. 12 and 22.

$$f^{K \mu_f \mu_i}(\Omega_i, \Omega_f, \omega_{23}) = \sum_{MM'Nnm} \langle LM \frac{1}{2} \mu_i | JN \rangle \langle JN | L'M'jn \rangle \langle jn | \ell m \frac{1}{2} \mu_f \rangle \times Y_L^{M*}(\theta, \Phi) Y_{L'}^{M'}(\frac{\pi}{2}, \psi_Y) Y_\ell^m(\frac{\pi}{2}, \psi_\Lambda), \quad (19)$$

where  $\psi_Y = \pi + \theta_1$ ,  $\psi_\Lambda = \pi + \theta_1 + \theta_1^*$ , and  $K \sim JLL'jl$ .

For "σ" and "ρ" type waves, a slightly different form is required:

$$f^{K \mu_f \mu_i}(\Omega_i, \Omega_f, \omega_{12}) = \sum_{MM'jlm} \langle LM \frac{1}{2} \mu_i | JN \rangle \langle JN | f^m \ell m \rangle \langle f^m | L'M' \frac{1}{2} \mu_f \rangle \times Y_L^{M*}(\theta, \Phi) Y_{L'}^{M'}(\frac{\pi}{2}, \psi_\sigma) Y_\ell^m(\frac{\pi}{2}, \psi_2), \quad (20)$$

where  $\psi_\sigma = \pi$  and  $\psi_2 = \pi + \theta_2^*$ .  $f, m$  are the spin and projection resulting from coupling the spin of the  $\Lambda$  and the relative angular momentum between the  $\Lambda$  and  $\pi\pi$  system.

The amplitudes formed from these factors T and f were normalized according to Eqn. 6 of the text.

FOOTNOTES AND REFERENCES

\*Work done under the auspices of the U. S. Atomic Energy Commission.

1. R. Levi-Setti, in Proceedings of the Lund International Conference on Elementary Particles, G. von Dardel. Ed. (Berlingska Boktryckeriet, Lund, Sweden, 1969), p. 339; E. Burkhardt, H. Filthuth, E. Kluge, H. Oberlack, R. R. Ross, B. Conforto, D. M. Harmsen, T. Lasinski, R. Levi-Setti, M. Raymond, R. Armenteros, M. Ferro-Luzzi, D. W. G. S. Leith, A. Minten, R. D. Tripp, R. Barloutaud, P. Granet, J. Meyer, and J. P. Porte, Nucl. Phys. B14, 106 (1969).
2. D. E. Plane, P. Baillon, C. Bricman, M. Ferro-Luzzi, J. Meyer, E. Pagiola, N. Schmitz, E. Burkhardt, H. Filthuth, E. Kluge, H. Oberlack, R. Barloutaud, P. Granet, J. P. Porte, and J. Prevost, Nucl. Phys. B22, 93 (1970).
3. Shu-bon Chan et al., in Hyperon Resonances-70, F. C. Fowler, Ed. (Moore Publishing Co., Durham, N. C., 1970), p. 79; also, D. Cline et al., Lettere al Nuovo Cimento 2, 407 (1969).
4. J. H. Bartley, R. Y. L. Chu, R. M. Dowd, A. F. Greene, J. Schneps, W. H. Sims, J. R. Albright, E. B. Brucker, J. E. Lannutti, B. G. Reynolds, M. Meer, J. E. Mueller, M. Schneiberger, and S. E. Wolf, Phys. Rev. Letters 21, 1111 (1968).
5. E. Burkhardt, H. Filthuth, E. Kluge, H. Oberlack, R. Armenteros, M. Ferro-Luzzi, D. W. G. S. Leith, R. Levi-Setti, J. Meyer, A. Minten, R. Barloutaud, P. Granet, J. P. Porte, Nucl. Phys. B27, 64 (1971).

6. J. Prevost et al., Partial Wave Analysis of  $\bar{K}N \rightarrow \Sigma(1385) \pi$  Between 0.6 and 1.2 GeV/c, paper presented by R. Barloutaud to the Amsterdam International Conference on Elementary Particles, June 30-July 6, 1974.
7. M. B. Watson, M. Ferro-Luzzi, and R. D. Tripp, Phys. Rev. 131, 2248-2281 (Sept. 1963).
8. Roger O. Bangerter, K-65 Beam Optics, Lawrence Radiation Laboratory, Alvarez Group Physics Note No. 574, Oct. 1965 (unpublished).
9. T. S. Mast, L. K. Gershwin, M. Alston-Garnjost, R. O. Bangerter, A. Barbaro-Galtieri, J. J. Murray, F. T. Solmitz, and R. D. Tripp, Phys. Rev. 183, 1200 (1969).
10. Stephen E. Derenzo and Roger H. Hildebrand, The Estimation of Scanning Efficiencies for Experiments Using Visual Detectors, Lawrence Radiation Laboratory Report UCRL-48638, Dec. 1968.
11. Roger Bangerter and Terry Mast, "Scan Efficiencies from Multiple Scans" Lawrence Berkeley Laboratory Alvarez Group Physics Note #731, Oct. 1971 (unpublished).
12. R. Armenteros, P. Baillon, C. Bricman, M. Ferro-Luzzi, E. Pagiola, J. O. Petersen, D. E. Plane, N. Schmitz, E. Burkhardt, H. Filthuth, E. Kluge, H. Oberlack, R. R. Ross, R. Barloutaud, P. Granet, J. Meyer, J. P. Porte, and J. Prevost, Nucl. Phys. B21, 15-76 (1970).
13. D. Morgan, Phys. Rev. 166, 1731 (1968); D. Morgan and G. Shaw, Phys. Rev. 2D, 520 (1970).
14. B. Deler and G. Valladas, Nuovo Cimento 45A, 559 (1966).

15. Particle Data Group, Reviews of Modern Physics 43, 2, Part II (April 1971). The decay asymmetry parameter is  $0.645 \pm 0.016$ . We have assumed the S and P-wave amplitudes are relatively real; neglecting the small relative phase of  $-6.3 \pm 3.5$  degrees.
16. Philippe H. Eberhard and Werner O. Koellner, The Optime System for Fitting Theoretical Expressions and Users Manual for the Optime System, Lawrence Radiation Laboratory Reports UCRL-20159 (Oct. 1970) and UCRL-20160 (Feb. 1981). The accuracy of the coding of the amplitudes and the relevant kinematics into the fitting program was checked in a variety of ways. The isobar-model amplitudes were calculated for a set of standard events and compared with the amplitudes calculated by other programs independently coded at Lawrence Berkeley Laboratory, Berkeley; SLAC, Stanford; and CEN, Saclay. In addition, Monte Carlo events were used to generate a variety of mass and angular distributions for each wave of Table III, and these were checked to be physically consistent with the quantum numbers. The polarization calculations were checked explicitly by hand for several events.
17. Particle Data Group, Reviews of Modern Physics 43, 2, Part II (April 1971).
18. The following masses were used to calculate the mixing angle;  $m_N = 1515 \pm 15$ ,  $m_\Sigma = 1670 \pm 10$ ,  $m_\Lambda = 1690 \pm 10$ ,  $m_\Xi = 1832 \pm 37$ ,  $m_\Lambda = 1518 \pm 2$  MeV.
19. R. Barloutaud (private communication).

20. The analysis of Ref. 5 uses an expression for this ratio which yields 3.3. We believe that the expression incorrectly normalizes the Breit-Wigner weight used to calculate an average  $\Sigma(1385)$  momentum over the Dalitz plot. The normalization of this weight should be independent of the incident momentum. If this change is made, their expression yields a result consistent with ours.
21. See, for example, R. H. Dalitz, in Symmetries and Quark Models, R. Chand, Ed. (Gordon and Breach, New York 1970).
22. David Fairman and Archibald Hendry, Physical Review **173**, 1720 (1968); Phys. Rev. **180**, 1572 (1969); David Fairman, Nuclear Physics **32B**, No. 2, 573(1971).
23. B. R. Martin and M. Sakitt, Physical Review **183**, 1352 (1969).
24. The results of this experiment have been briefly described in Lawrence Berkeley Laboratory Report #300 (submitted to Physical Review Letters).

Table I. Partial cross sections for  $K^- p \rightarrow \Lambda \pi^+ \pi^-$  with statistical errors only.

Momentum (MeV/c)	Cross section $\sigma$ (mb)	Weighted $\Lambda \pi^+ \pi^-$ events
295	$0.32 \pm .17$	7
305	$0.21 \pm 0.09$	11
315	$0.19 \pm 0.07$	17
325	$0.32 \pm 0.07$	39
335	$0.35 \pm 0.07$	47
345	$0.61 \pm 0.10$	77
355	$0.67 \pm 0.06$	195
365	$1.05 \pm 0.06$	717
375	$1.77 \pm 0.06$	1863
385	$2.64 \pm 0.08$	3491
395	$2.93 \pm 0.09$	3298
405	$2.33 \pm 0.09$	2114
415	$1.80 \pm 0.09$	982
425	$1.46 \pm 0.11$	338
435	$1.41 \pm 0.15$	200
445	$1.41 \pm 0.17$	151
455	$1.45 \pm 0.23$	84
465	$1.97 \pm 0.52$	30

Table II. Variables used in isobar-model partial-wave analysis.

$\mu_i, \mu_f$	= Initial proton and final lambda spin projections
L, M	= Initial $K^- p$ angular momentum and projection
J, N	= Initial $K^- p$ total spin and projection
$L', M'$	= Angular momentum and projection between isobar and third particle
j, n	= Spin and projection of the isobar
$\ell, m$	= Angular momentum and projection between isobar decay particles
$P_1, P_2, P_3$	= Momentum of particles 1, 2, 3 in the overall c.m.
$P_1'$	= Momentum of particle 2 or 3 in the rest frame of particles 2 and 3
E	= Total energy in the three-particle rest frame
$m_{ij}$	= Invariant mass of particles i and j
$\Omega_i = \Theta, \Phi$	= Polar and azimuth of the incident beam with respect to the normal to the three-particle plane. The azimuth is defined from the lambda direction
$\Omega_f = \frac{\pi}{2}, \psi_Y$	= Polar and azimuth of the isobar with respect to the normal to the three-particle plane
$\omega_{23} = \frac{\pi}{2}, \psi_\Lambda$	= Polar and azimuth of the lambda with respect to the normal to the three-particle plane
$\theta_1, \theta_2$	= Angle between pion 1, 2 and the lambda
$\theta_1^*, \theta_2^*$	= Angle between the lambda and isobar in the isobar rest frame
$\mu_p$	= Spin projection of the lambda-decay proton
$\theta, \psi$	= Polar and azimuthal angles of the lambda-decay proton in the lambda rest frame

Table III. Waves used in partial-wave analysis.

K	TYPE	LL'12J
1	$Y^*$	DS03
2		DS13
3		PP01
4		PP11
5		PP03
6		PP13
7	$-\Delta\pi$	PS01
8		PS11
9		SP01
10		SP11
11		DP03
12		DP13
13	$\sigma$	PS01
14		SP01
15		DP03
16	$\rho$	SS11
17		DS13

All angles are defined in the three-particle rest frame except those which are starred, which are defined in the appropriate diparticle rest frame.

Table IV. Events used in partial-wave analysis.

Bins	Momentum (MeV/c)	Number of events	Weighted number of events
1	350-360	129	164.5
2	360-370	484	597.0
3	370-380	1312	1570.5
4	380-390	2494	3073.2
5	390-400	2197	2718.8
6	400-410	1384	1717.7
7	410-420	615	750.0
8	420-440	314	383.8
9	440-470	163	191.6

Table V. Amplitudes from the isobar-model fit at each momentum. In the fitting the Y\* DS03 amplitude was fixed real. For the Argand plots of Fig. 13 the amplitudes have been rotated by  $\delta$ , the phase of the Breit-Wigner discussed in the text.

Momentum Interval (MeV/c)	Y* DS03		Y* DS13		Y* PP01		Y* PP03		$\sigma$ P501		$\sigma$ DP03		$\delta$
	Re	Im	Re	Im	Re	Im	Re	Im	Re	Im	Re	Im	
350-360	.034 .002	.000 .000	-.016 .006	-.021 .010	-.011 .008	-.011 .009	.009 .007	-.007 .009	.048 .015	-.021 .016	-.005 .008	-.010 .008	.437
360-370	.062 .002	.000 .000	-.007 .002	-.010 .007	-.029 .004	-.005 .009	.003 .004	.004 .006	.047 .005	.000 .010	-.000 .003	-.004 .007	.593
370-380	.079 .001	.000 .000	-.006 .002	.010 .005	-.020 .003	.014 .007	.006 .003	-.000 .004	.051 .004	-.032 .006	.011 .003	.008 .005	.869
380-390	.103 .002	.000 .000	-.004 .002	.011 .004	-.026 .003	.038 .006	-.002 .003	.016 .004	.028 .003	-.031 .005	.018 .003	.005 .004	1.239
390-400	.109 .002	.000 .000	.002 .002	-.000 .004	-.002 .003	.040 .006	.005 .003	.006 .004	.002 .004	-.051 .005	.026 .003	.005 .004	1.703
400-410	.102 .002	.000 .000	.003 .002	.003 .005	.016 .004	.034 .007	.007 .004	.009 .005	-.017 .005	-.056 .006	.013 .004	.012 .005	2.055
410-420	.085 .002	.000 .000	.003 .003	.006 .006	.016 .006	.039 .009	.001 .006	.001 .006	-.034 .007	-.053 .008	.014 .005	.006 .005	2.281
420-440	.060 .002	.000 .000	.009 .005	-.010 .009	.026 .010	.035 .011	.003 .008	.010 .009	-.050 .014	-.066 .013	.021 .008	-.005 .008	2.472
440-470	.055 .003	.000 .000	.020 .008	-.007 .012	.052 .014	.015 .021	.013 .013	-.003 .014	-.070 .014	-.042 .022	.028 .012	-.018 .012	2.641

Table VI. Chi-squares from the  $\Lambda\pi^+$ ,  $\Lambda\pi^-$ , and  $\pi^+\pi^-$  mass projections.

Momentum interval (MeV/c)	$\Lambda\pi^+$	$\Lambda\pi^-$	$\pi^+\pi^-$
350-360	11.0	3.7	10.4
360-370	14.8	17.5	21.1
370-380	11.4	11.0	40.1
380-390	22.6	16.9	28.1
390-400	25.1	19.8	33.7
400-410	9.2	13.7	20.5
410-420	19.0	12.8	21.1
420-440	8.7	15.7	44.5
440-470	5.7	28.3	14.2
<b>Total</b>	<b>128</b>	<b>139</b>	<b>234</b>
<b>Total data points</b>	<b>113</b>	<b>113</b>	<b>207</b>

Table VII. Properties of  $J^P = 3/2^-$  baryons.\*

Resonance	Mass MeV	Total width MeV	Decay modes	Branching fraction X	Remarks
$\Lambda(1520)$	$1518 \pm 2$	$16 \pm 2$	$N\bar{K}$ $\Sigma\pi$ $\Sigma(1385)\pi$	$0.46 \pm 0.01$ $0.41 \pm 0.01$ $0.093 \pm 0.006$	
$\Lambda(1690)$	$1690 \pm 10$	27 to 85	$N\bar{K}$ $\Sigma\pi$ $\Sigma(1385)\pi$	$\sim 30$ $\sim 40$ $0.005$ to $0.04$	
$N(1520)$	1510 to 1540	105 to 150	$N\pi$ $N\pi\pi$ $N\eta$	$\sim 50$ $\sim 50$ $\sim 0.6$	Dominated by $\Delta(1236)\pi$
$\Sigma(1670)$	1660 to 1680	$50 \pm 10$	$N\bar{K}$ $\Sigma\pi$ $\Lambda\pi$ $\Sigma(1385)\pi$	$\sim 0.08$	The experimental situation is confused. There is probably more than one $3/2^-$ state. $X_{N\bar{K}} X_{\Sigma(1385)\pi} = 0.031 \pm 0.006$
$\Xi(1820)$	1795 to 1870	50 to 100	$\Xi\pi$ $\Sigma\bar{K}$ $\Lambda\bar{K}$		
$\Delta(1670)$	1650 to 1720	175 to 300	$\Delta\pi$ $N\pi$	$0.15 \pm 0.03$	
$N(1700)$	1600 to 1730				Only poor evidence from partial-wave analysis
$\Sigma(1940)$	$1940 \pm 22$	$235 \pm 28$	$N\bar{K}$ $\Lambda\pi$ $\Sigma\pi$		$\sqrt{X_{N\bar{K}} X_{\Lambda\pi}} = .13 \pm .03$ $\sqrt{X_{N\bar{K}} X_{\Sigma\pi}} = .12 \pm .03$
$\Lambda(2010)$	1980 to 2040	80 to 180	$N\bar{K}$ $\Sigma\pi$		Seen in only one partial-wave analysis $\sqrt{X_{N\bar{K}} X_{\Sigma\pi}} = .20 \pm .04$
$N(2040)$	$2040 \pm 11$	$274 \pm 24$	$N\pi$	$0.17 \pm 0.06$	

\* From Ref. 17.

## FIGURE CAPTIONS

- Fig. 1. Pathlength (events/millibarn/10 MeV/c) as a function of incident  $K^-$  momentum (MeV/c).
- Fig. 2. Histogram of the error in the fitted  $K^-$  momentum in MeV/c.
- Fig. 3. Lambda lifetime distribution. Each event is plotted at  $(t-t_0)$  to remove the effect of the cut on short-length lambdas. The value of  $t_0$  for each event is described in the text. The straight line corresponds to the known lambda lifetime.
- Fig. 4. The partial cross section for  $K^-p \rightarrow \Lambda\pi^+\pi^-$  in millibarns as a function of incident momentum (MeV/c). The two dotted points are results from Ref. 12. The crossed points are the predictions for the background from the fit described in the text.
- Fig. 5. Dalitz plots for  $K^-p \rightarrow \Lambda\pi^+\pi^-$  at various incident  $K^-$  laboratory momenta. The abscissa (ordinate) corresponds to  $\Lambda\pi^+$  ( $\Lambda\pi^-$ ) invariant-mass-squared in  $\text{GeV}^2$ . Horizontal and vertical lines show  $M^2$  and  $(M-\Gamma)^2$  for the  $\Sigma(1385)$ .
- Fig. 6.  $\Lambda\pi^+$  invariant-mass-squared distribution for various incident  $K^-$  momenta. The solid lines connect the results of a Monte Carlo prediction from the isobar model described in the text.
- Fig. 7.  $\Lambda\pi^-$  invariant-mass-squared distribution for various incident  $K^-$  momenta. The solid lines connect the results of a Monte Carlo prediction from the isobar model described in the text.
- Fig. 8.  $\pi^+\pi^-$  invariant-mass-squared distribution for various incident  $K^-$  momenta. The solid lines connect the results of a Monte Carlo prediction from the isobar model described in the text.
- Fig. 9. The Dalitz plot asymmetry as a function of incident  $K^-$  momentum. The asymmetry is  $\alpha = (N^- - N^+) / (N^- + N^+)$ , where  $N^-$

- is the number of events with  $\Lambda\pi^-$  invariant mass larger than  $\Lambda\pi^+$  invariant mass. The dots are the predictions of the isobar-model fit described in the text.
- Fig. 10. The center-of-mass production cosine distribution of the lambda. The curves are the results of a Legendre polynomial expansion fit to the production angular distribution and polarization at each incident momentum.
- Fig. 11. The Legendre polynomial coefficients from the fit to the lambda production angular distribution and polarization. The dots correspond to the predictions of the isobar-model fit.
- Fig. 12. Schematic diagram of the isobar-model description of the reaction  $K^-p \rightarrow \Lambda\pi^+\pi^-$ . Particle 1, 2, and 3 refer to  $\pi^-$ ,  $\pi^+$ , and  $\Lambda$ . The notation is defined in Table II.
- Fig. 13. Argand plots of the amplitudes from the isobar-model fit. The number refers to the incident-momentum intervals defined in Table IV. The curve on the plot of  $Y^*DS03$  is the prediction of a Breit-Wigner amplitude for the  $\Lambda(1520)$ .
- Fig. 14. Partial cross sections (millibarns) for the only two waves with an incident D-wave. Both waves ( $Y^*DS03$  and  $\sigma DP03$ ) peak near 395 MeV/c, the momentum required to form the  $\Lambda(1520)$ . Note the difference in scales.
- Fig. 15. The ratio of the cross section for  $Y^*DS03$  to the sum of the cross sections for  $Y^*DS03$  and  $\sigma DP03$  as a function of incident momentum.
- Fig. 16. The integral of the  $Y^*DS03$  amplitude squared (I) and the integral of the  $\Lambda\pi^+\pi^-$  phase space ( $\rho$ ) as a function of incident  $K^-$  momentum in the region of the  $\Lambda(1520)$  and in the region of the  $\Lambda(1690)$ . The same (arbitrary) scale is used in both regions.

Fig. 17. Events weighted by  $e^{t/\tau}$  as a function of lambda projected length (cm). The sharp depletion of events with a projected length less than 0.25 cm corresponds to the loss of events with short-length lambdas.

Fig. 18. Scatter plot of the lambda decay cosine versus the lambda laboratory momentum (MeV/c). The lambda decay cosine is the angle between the lambda and the decay proton in the lambda rest frame. The depletion of events near low momentum and  $\cos\theta = -1.0$  shows the loss of events with short-length protons.

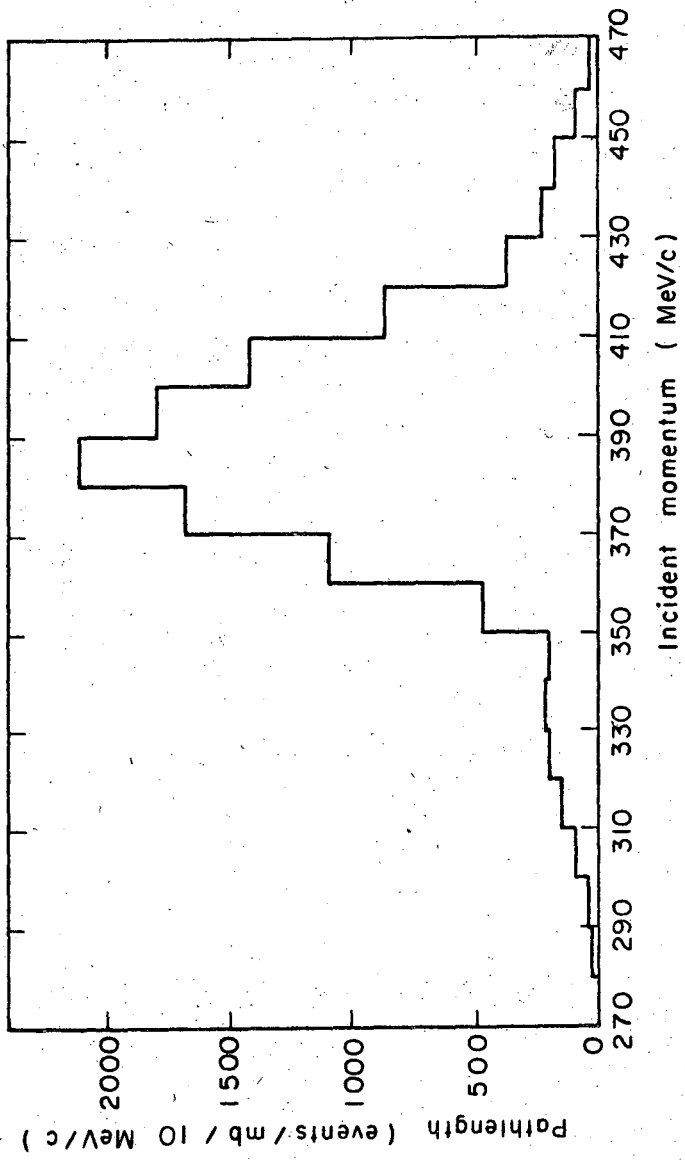
Fig. 19. Scatter plot of the lambda decay cosine versus the lambda laboratory momentum (MeV/c). The dashed lines indicate the boundaries of the "inner volume" used to investigate the deviation from isotropy of the lambda decay.

Fig. 20. The weight used to account for anisotropy of the lambda decay as a function of lambda laboratory momentum. No correction was made for events with momenta greater than 150 MeV/c and the small weight indicated by the straight line was applied for events with lower momenta.

Fig. 21. The distribution of the lambda production azimuth; values of 0 and  $\pi$  correspond to lambdas with a line of flight toward and away from the scanner. No significant deviation from isotropy is observed.

Fig. 22. Diagram defining the angles used in the isobar model. The notation is defined in Table II.





XBL 718 - 4208

Fig. 1

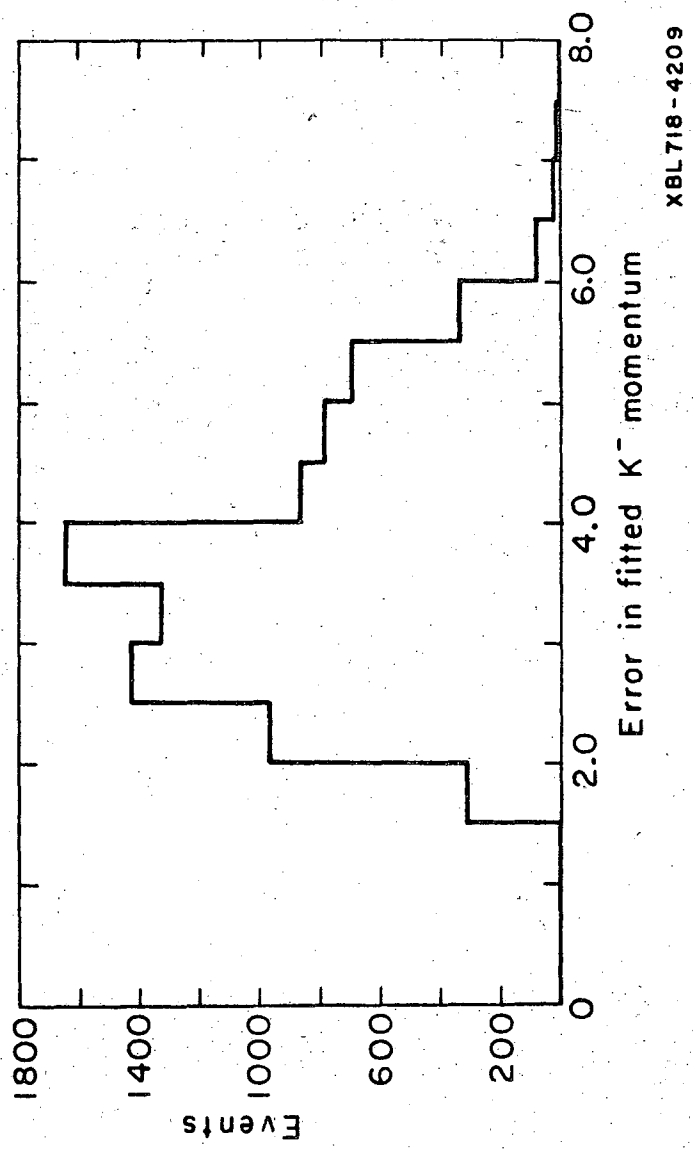


Fig. 2

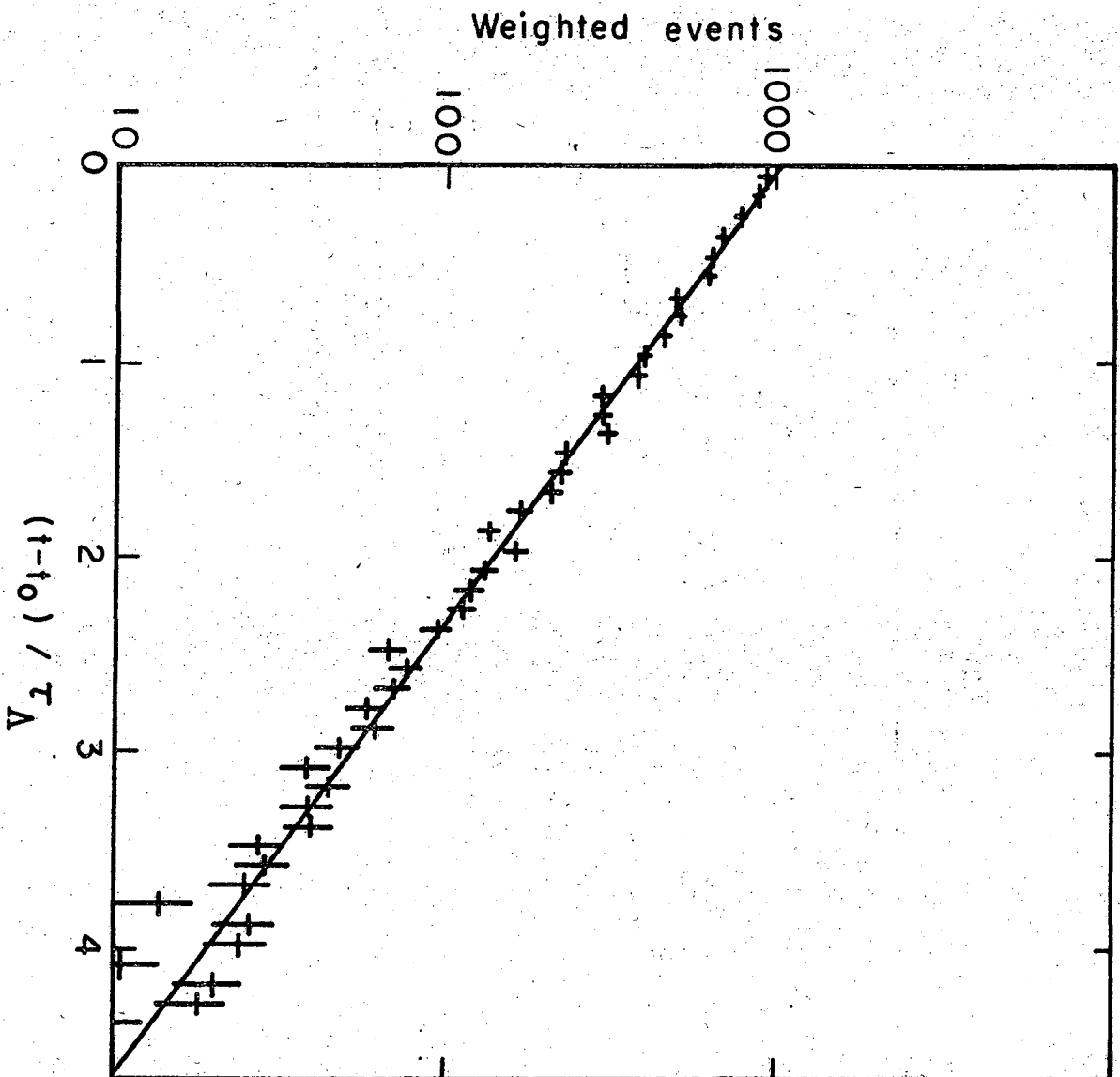
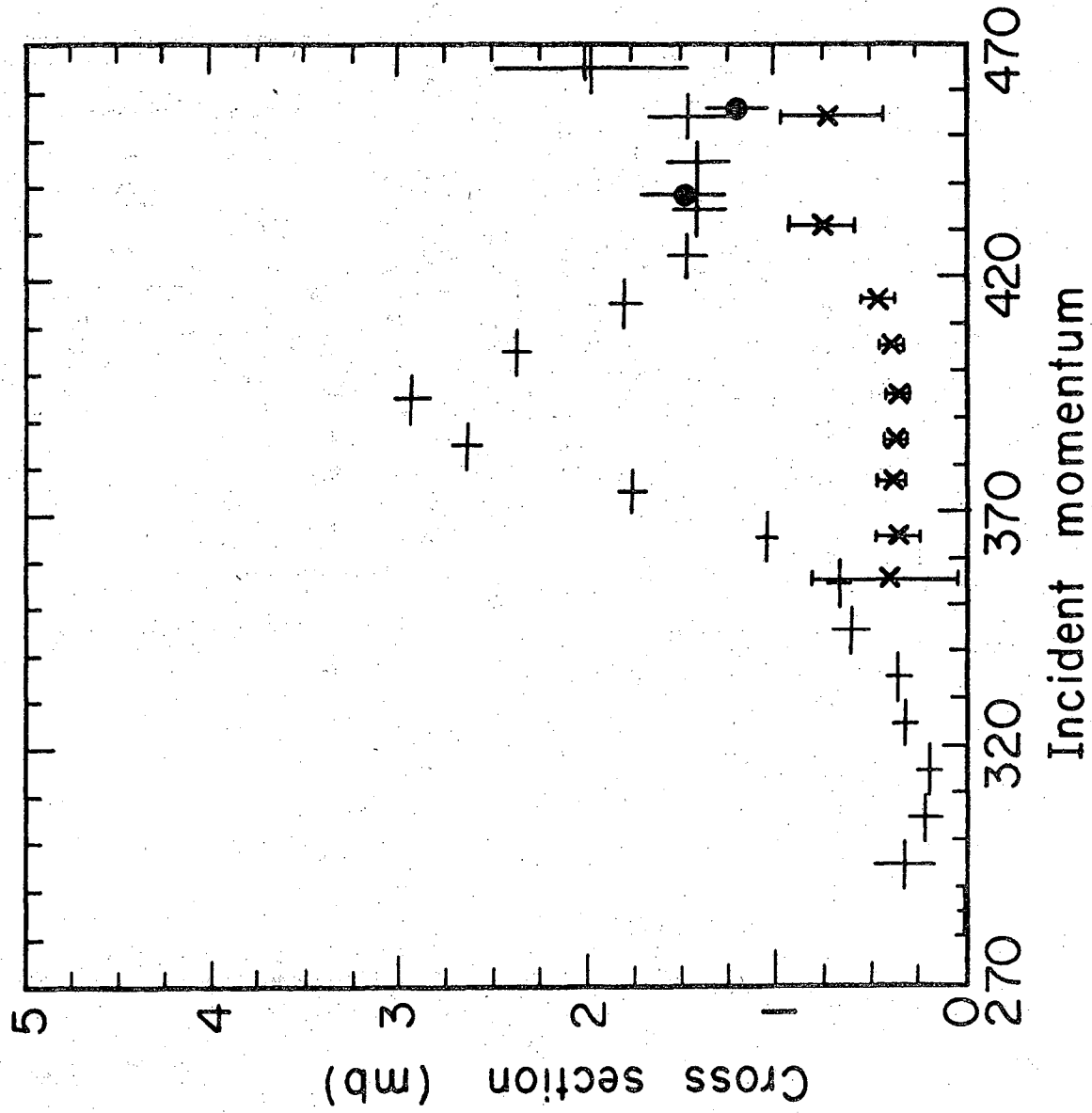


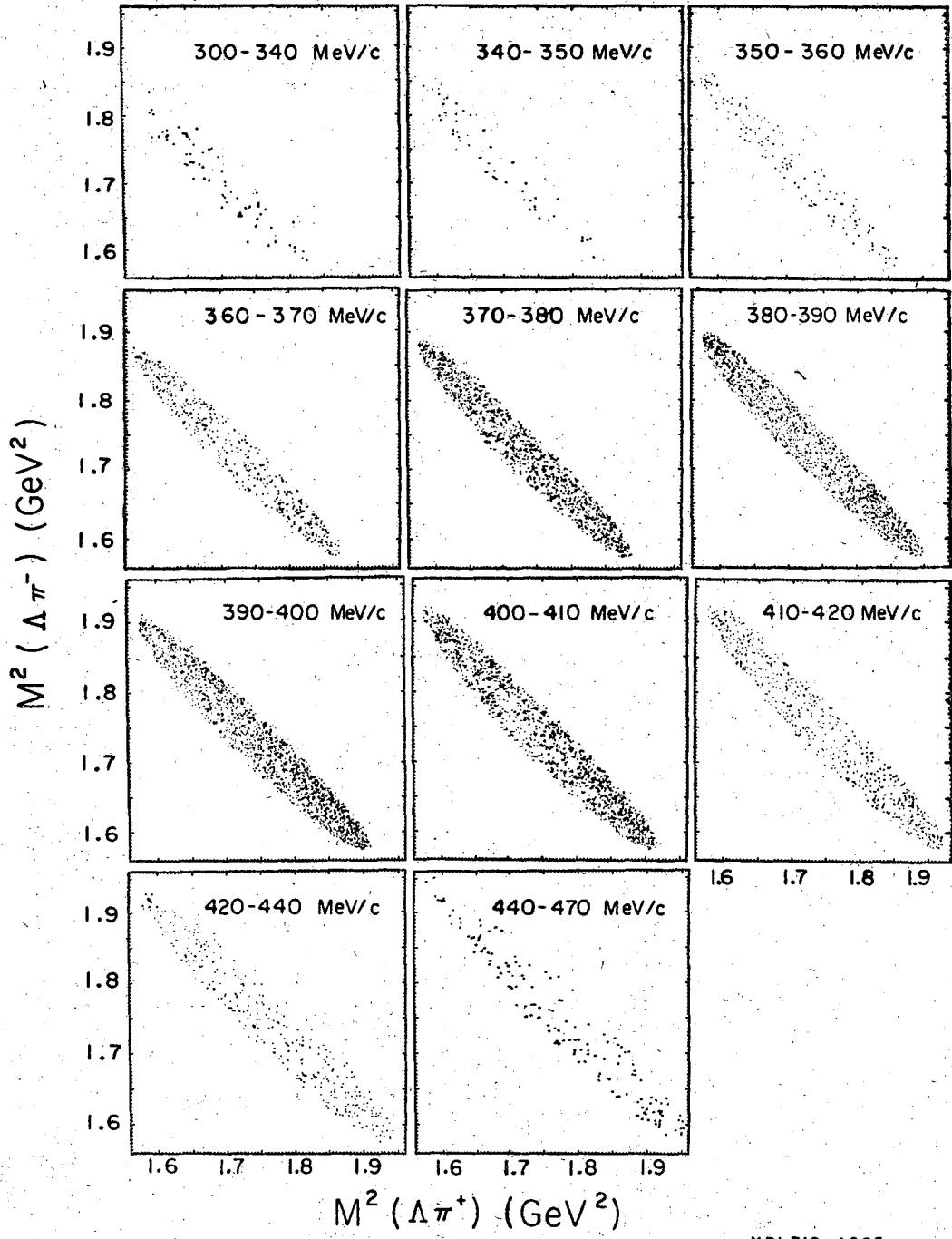
Fig. 3

XBL 718-4214



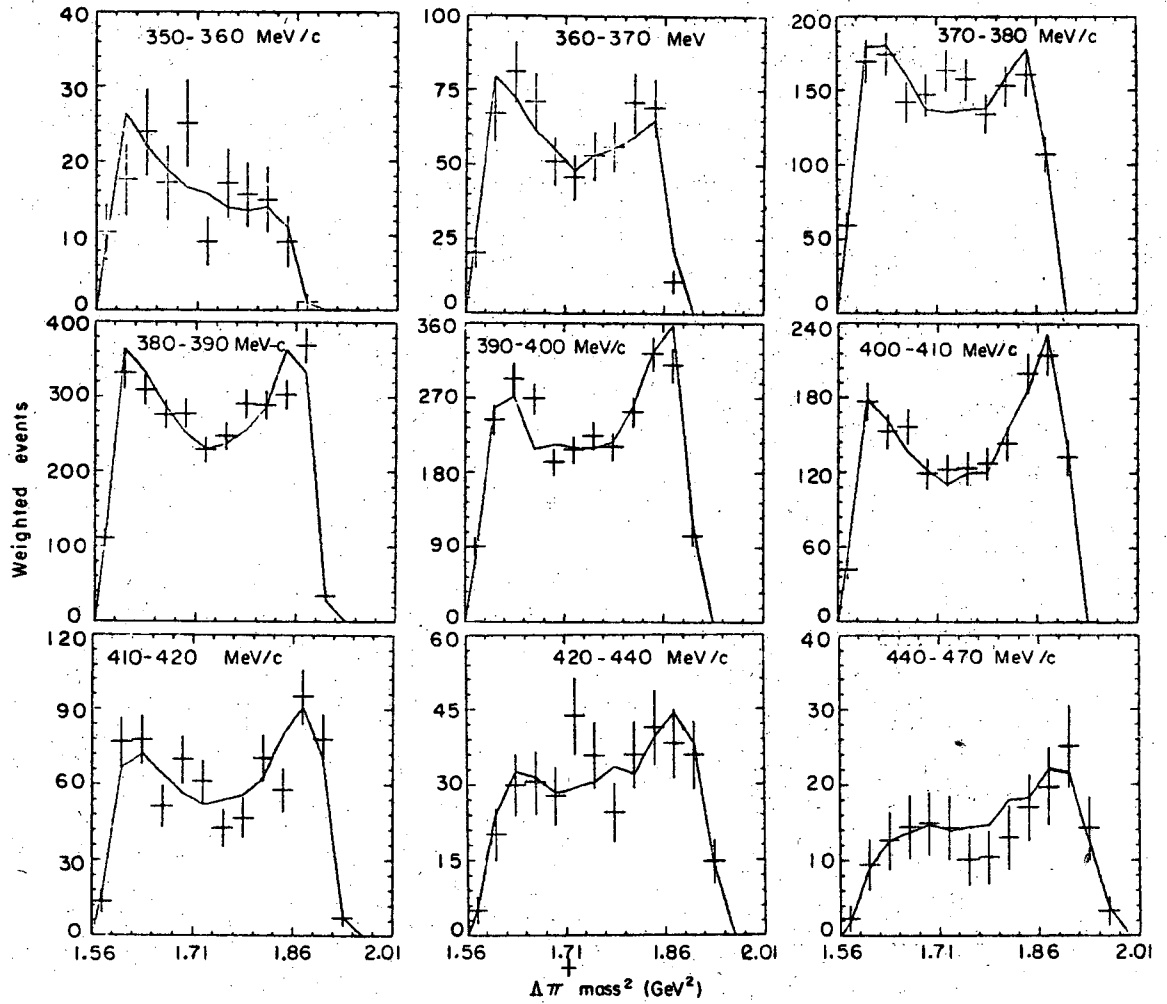
XBL718-4141

Fig. 4



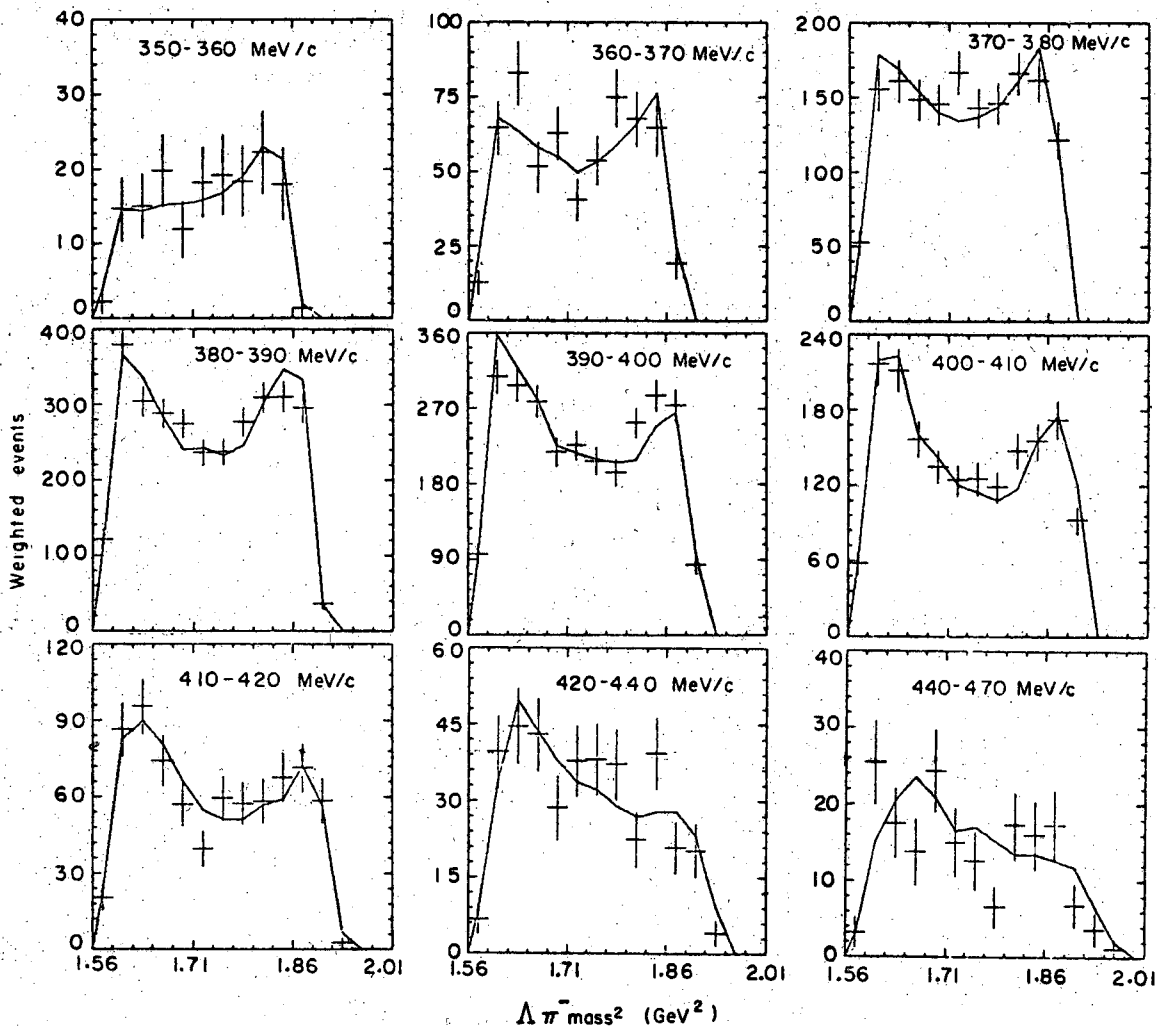
XBL718-4205

Fig. 5



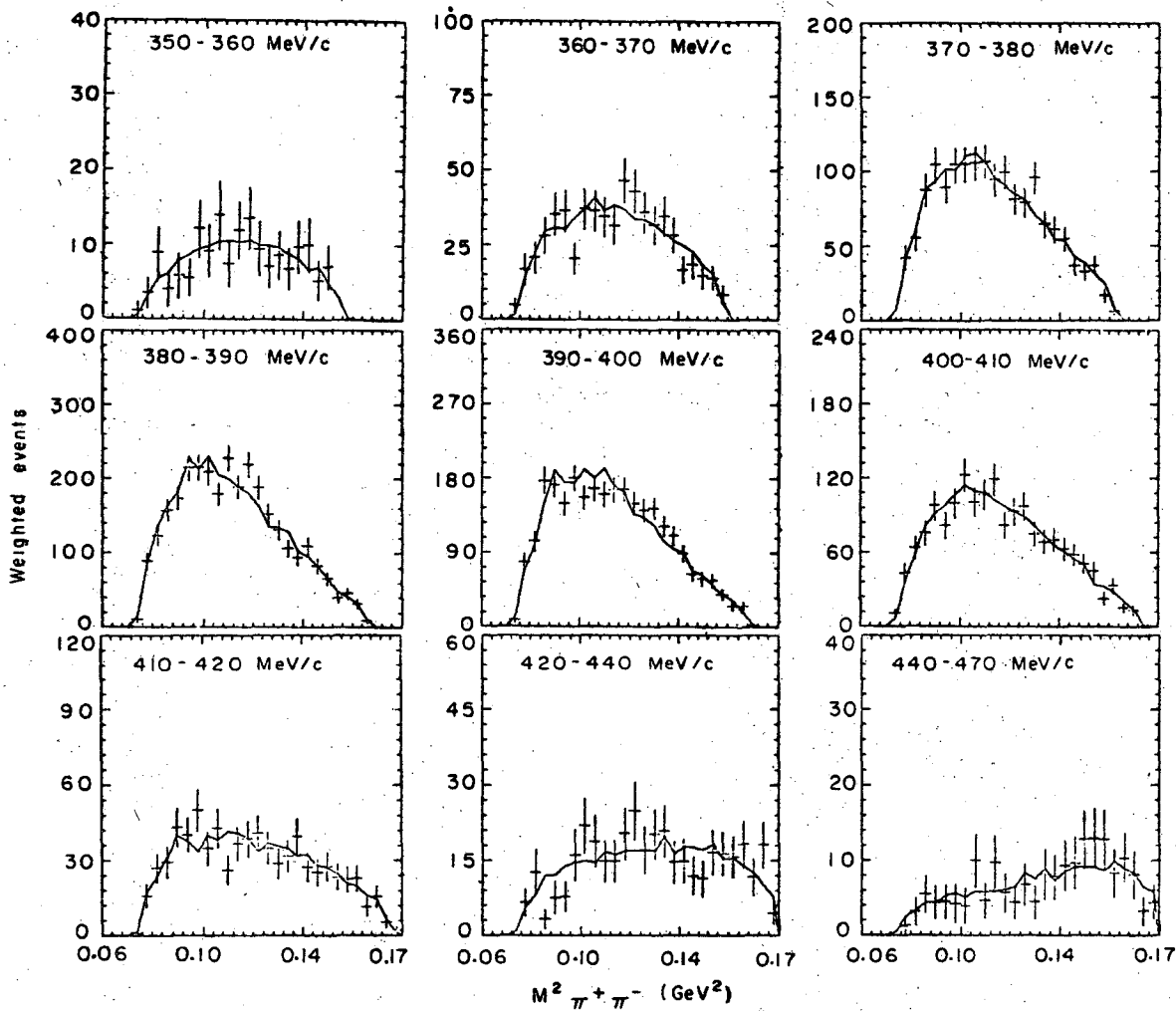
X BL 718-4218

Fig. 6



XBL718 -4220

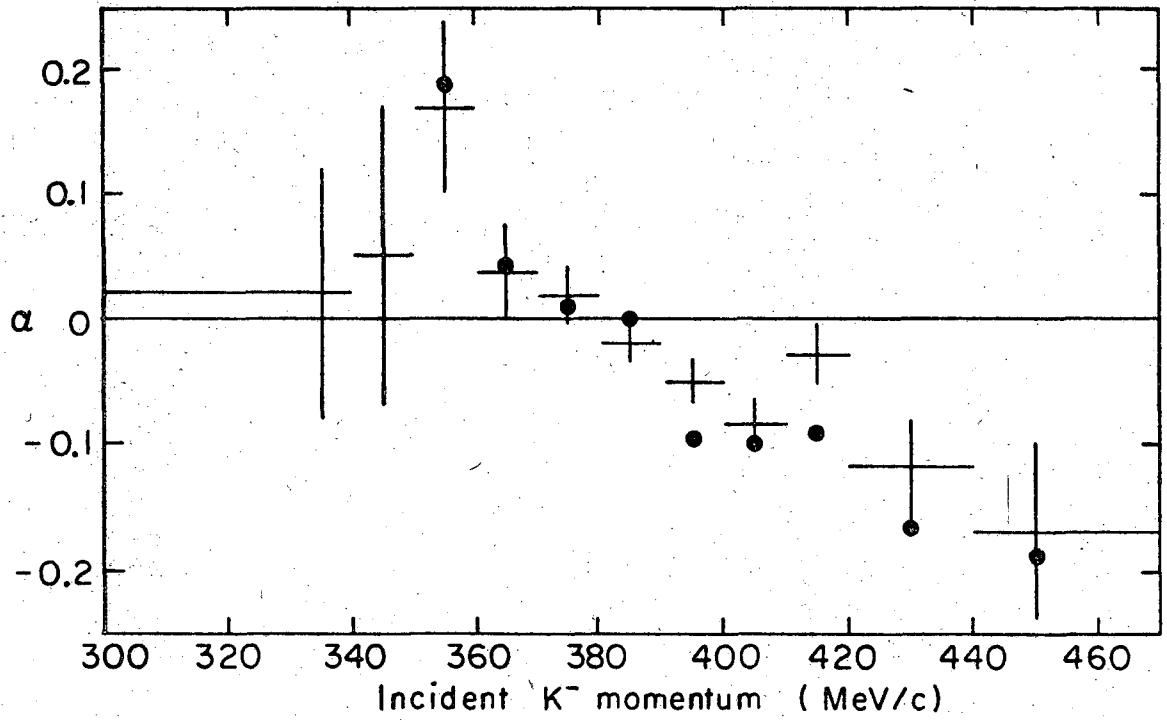
Fig. 7



XBL718-4219

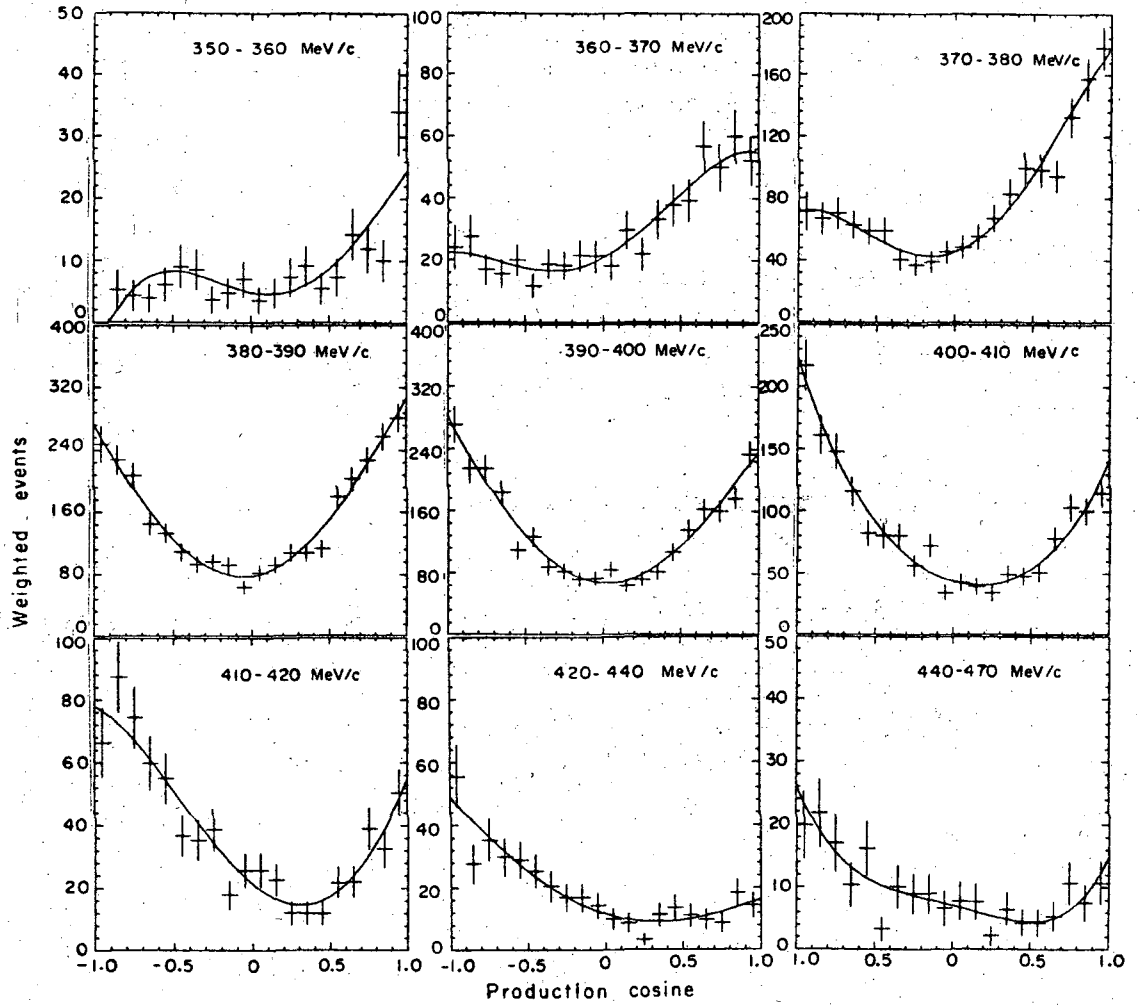
Fig. 8





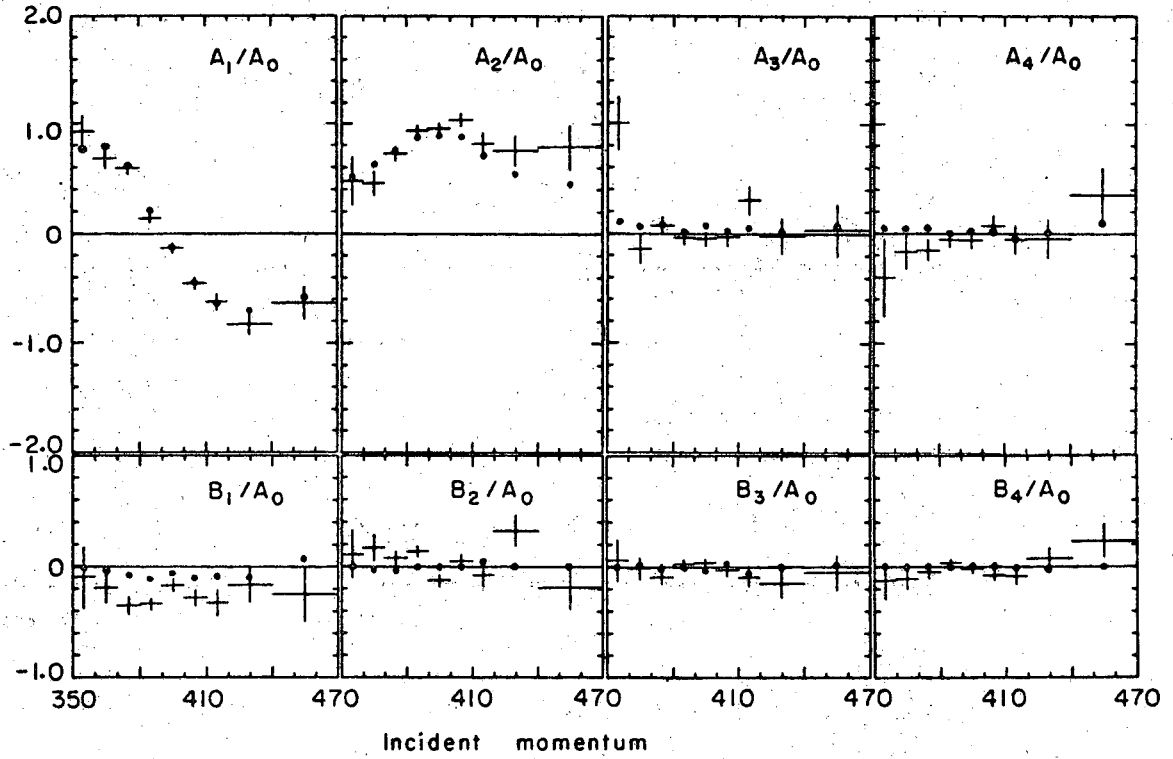
XBL 718 - 4216

Fig. 9



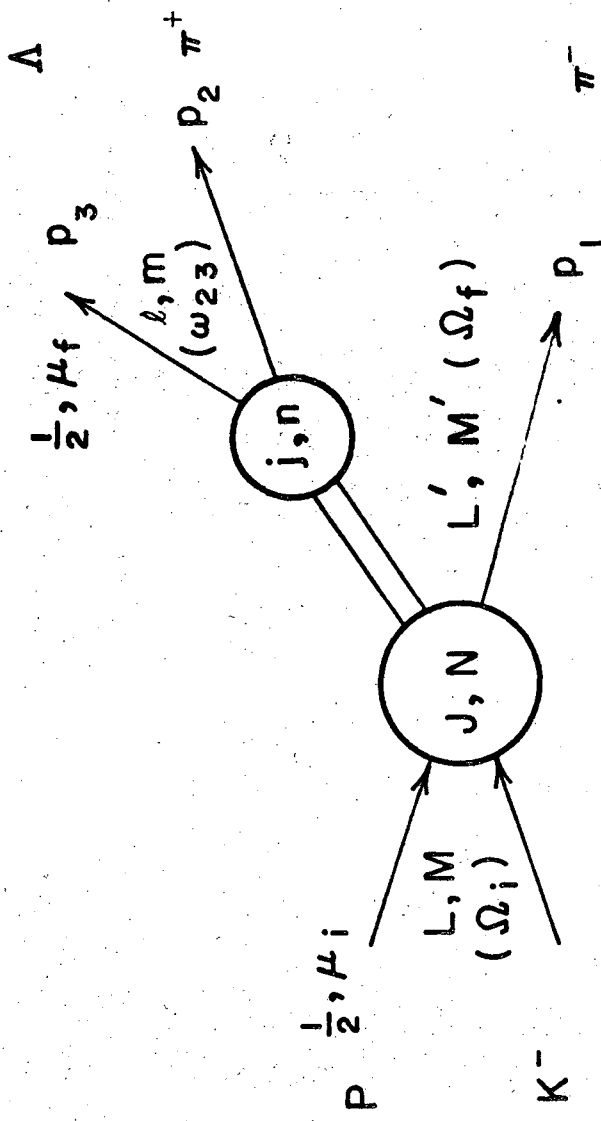
XBL718-4207

Fig. 10



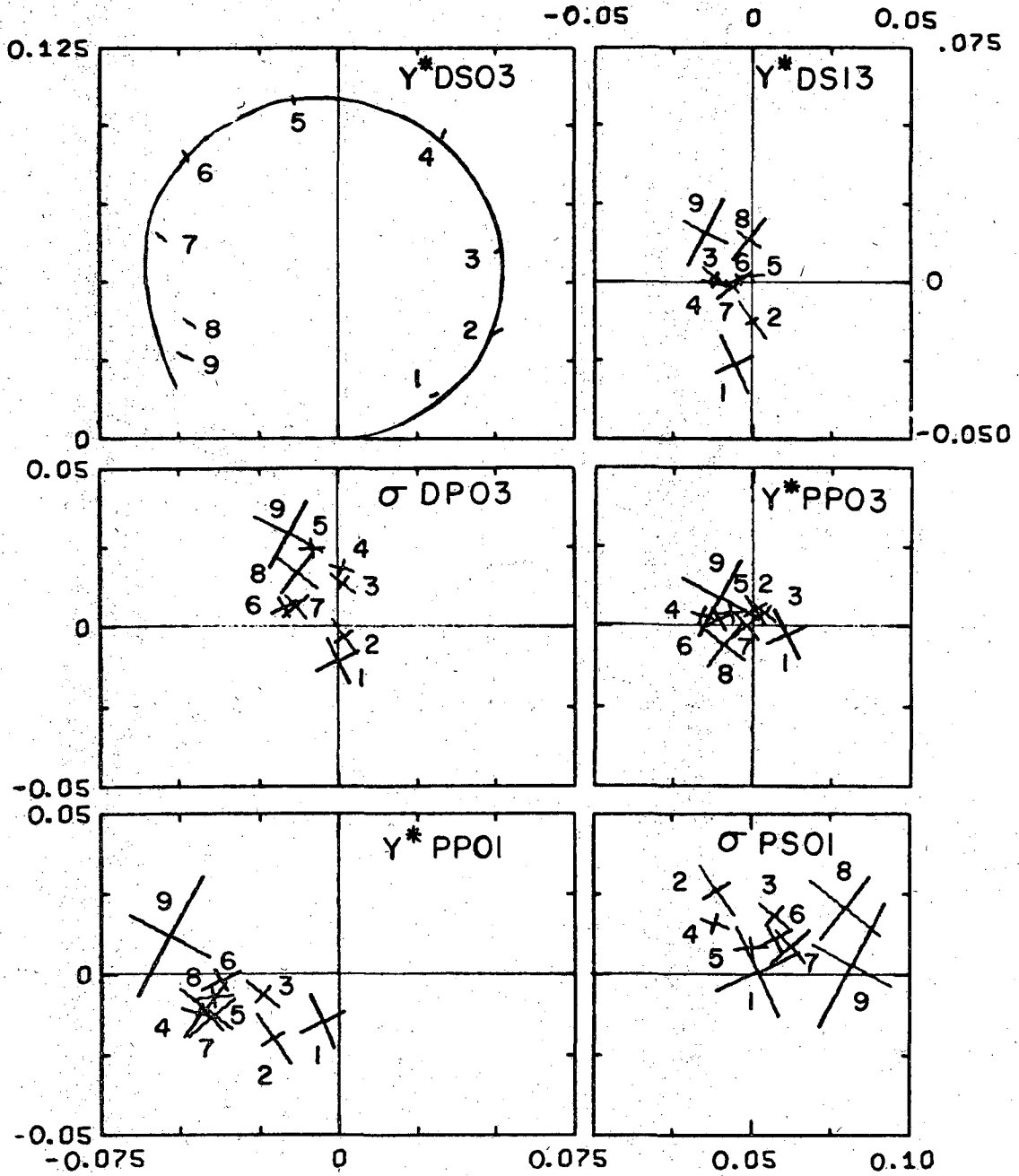
XBL718 - 4204

Fig. 11



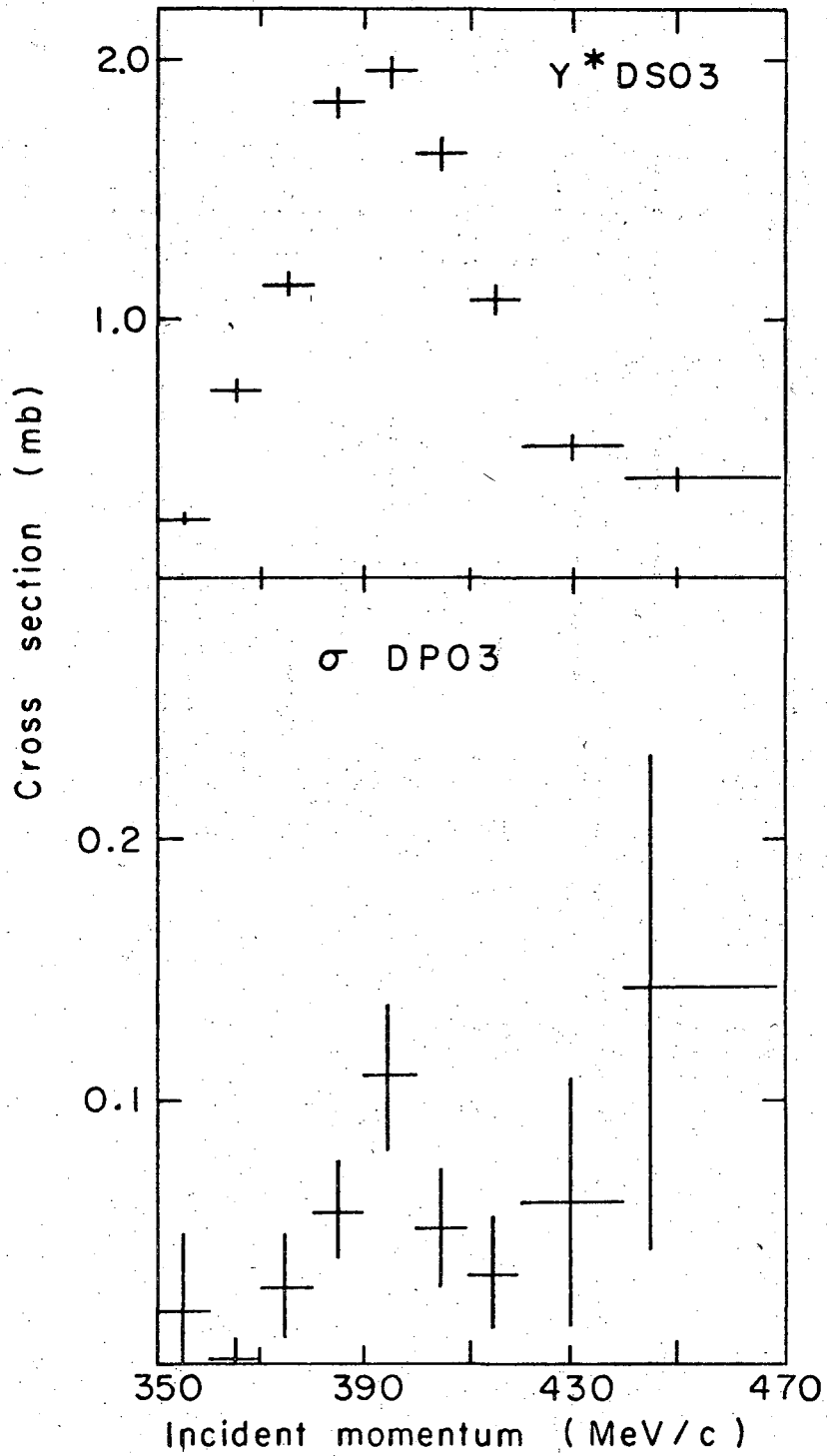
XBL718 - 4213

Fig. 12



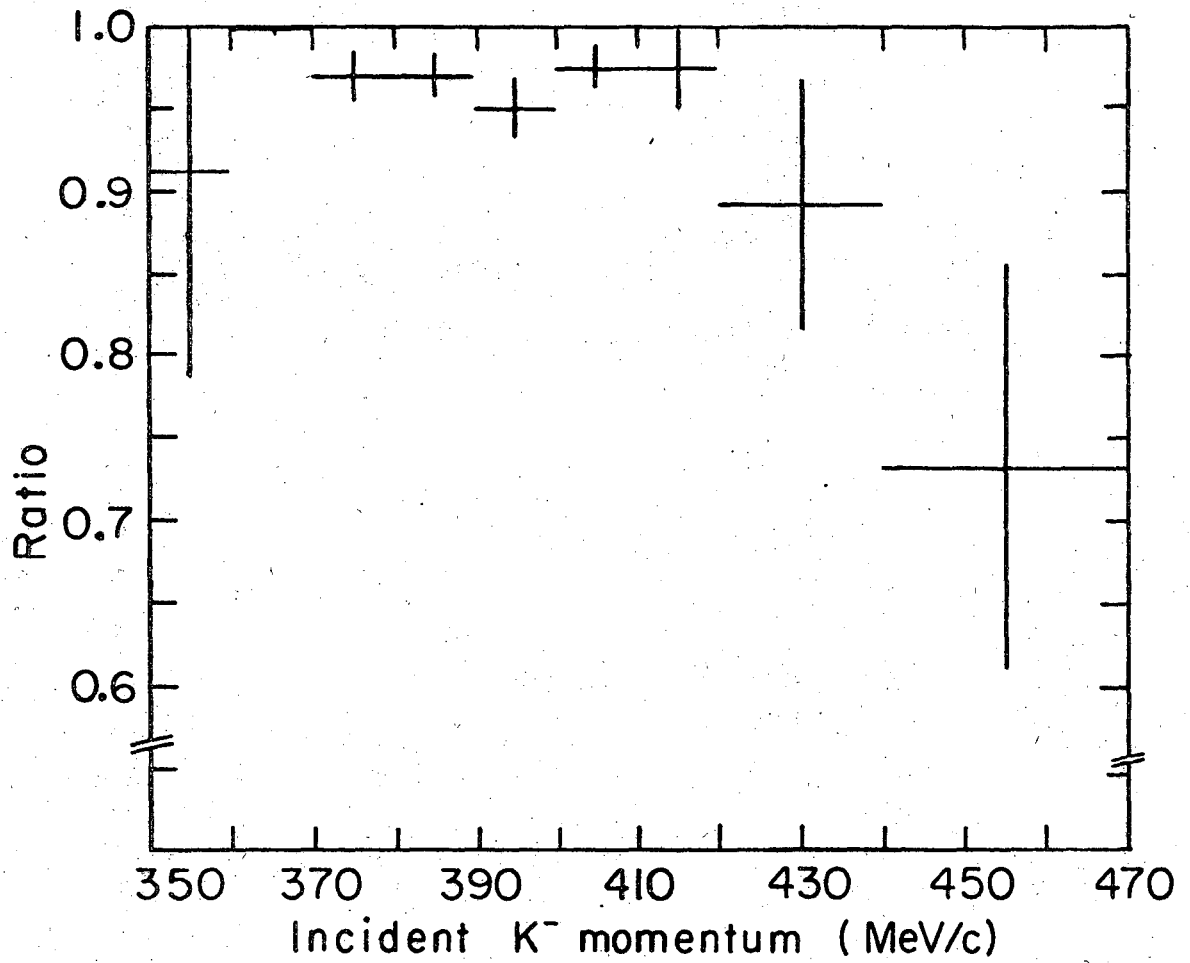
XBL7110-4527A

Fig. 13



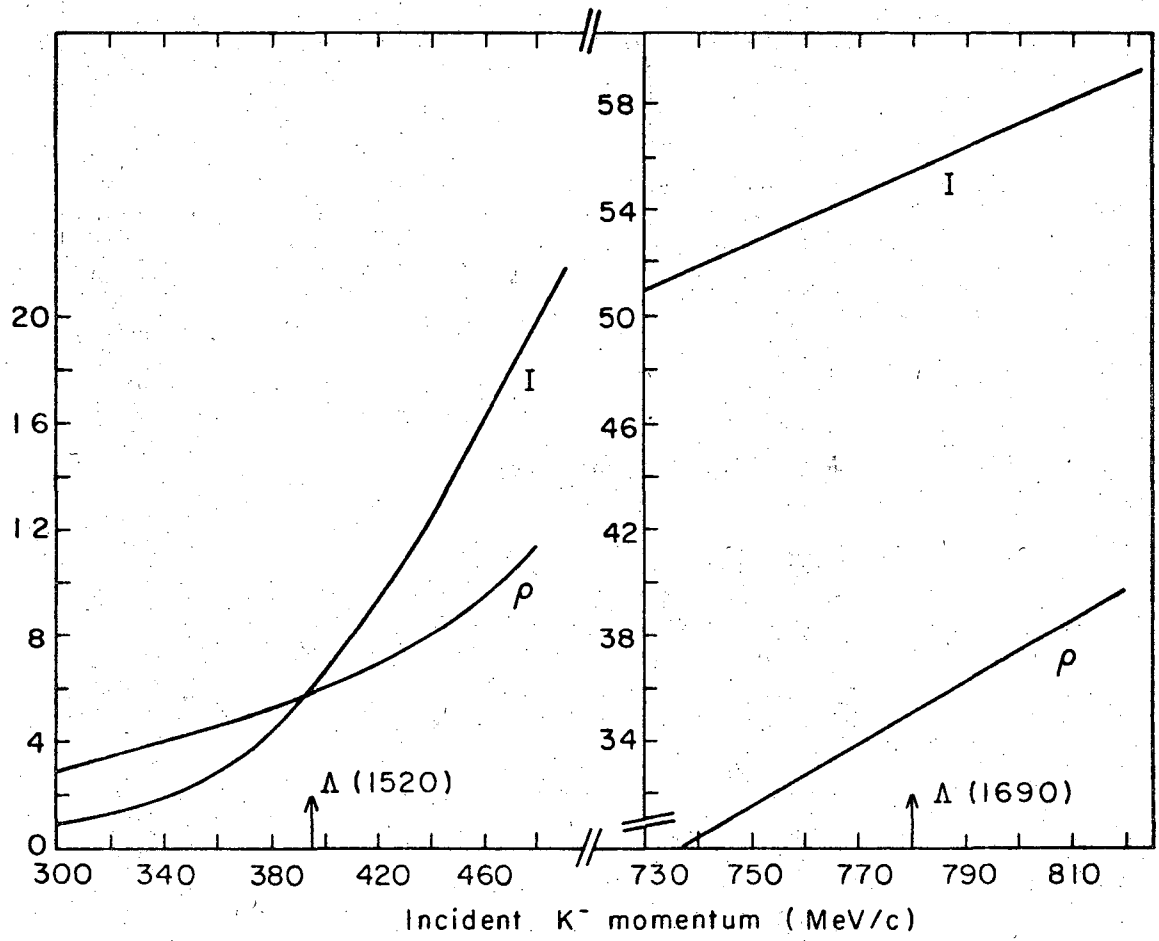
XBL718 - 4215

Fig. 14



XBL718 - 4211

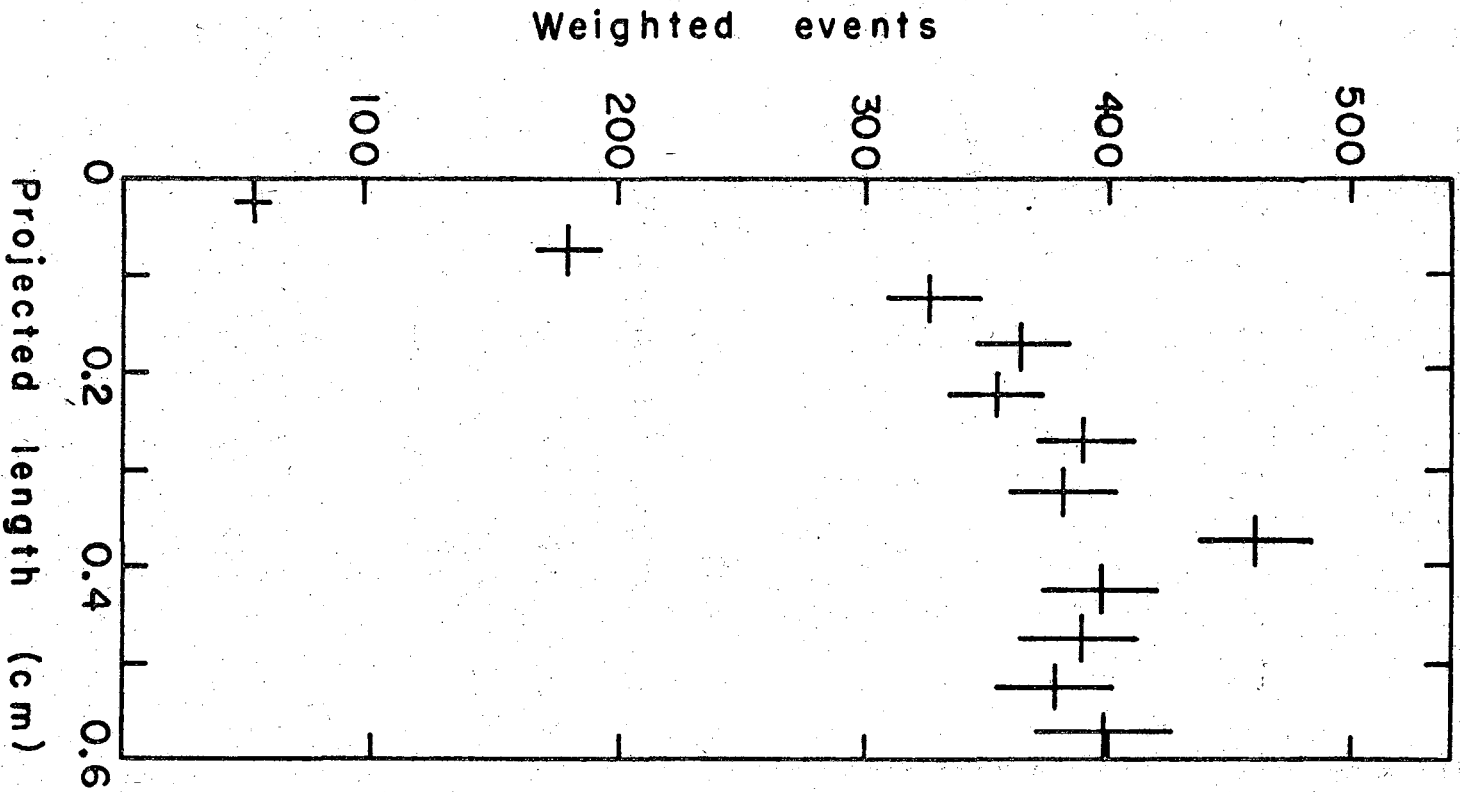
Fig. 15



XBL 718-4217

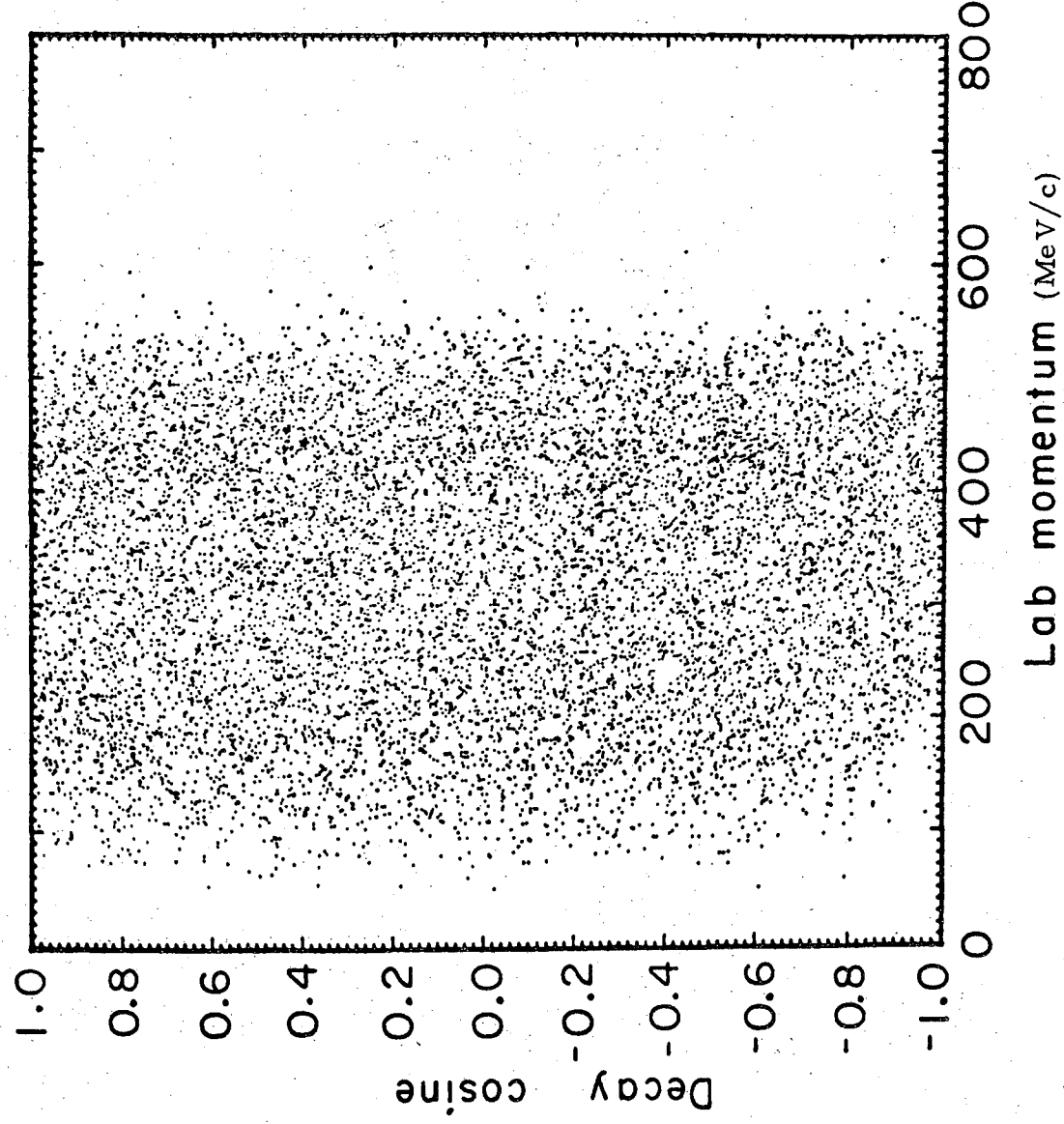
Fig. 16





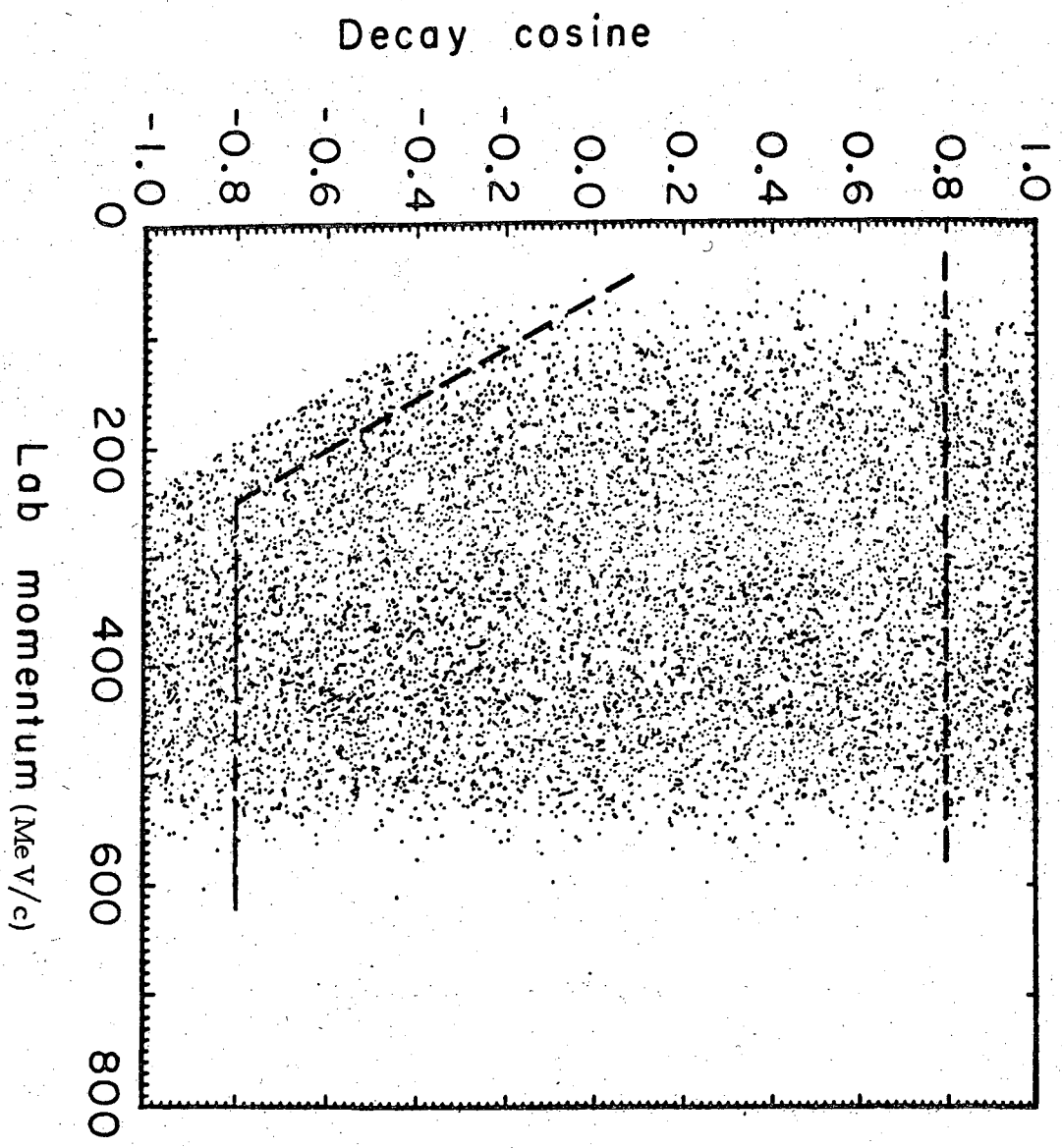
XBL 718 - 4 2 1 0

Fig. 17



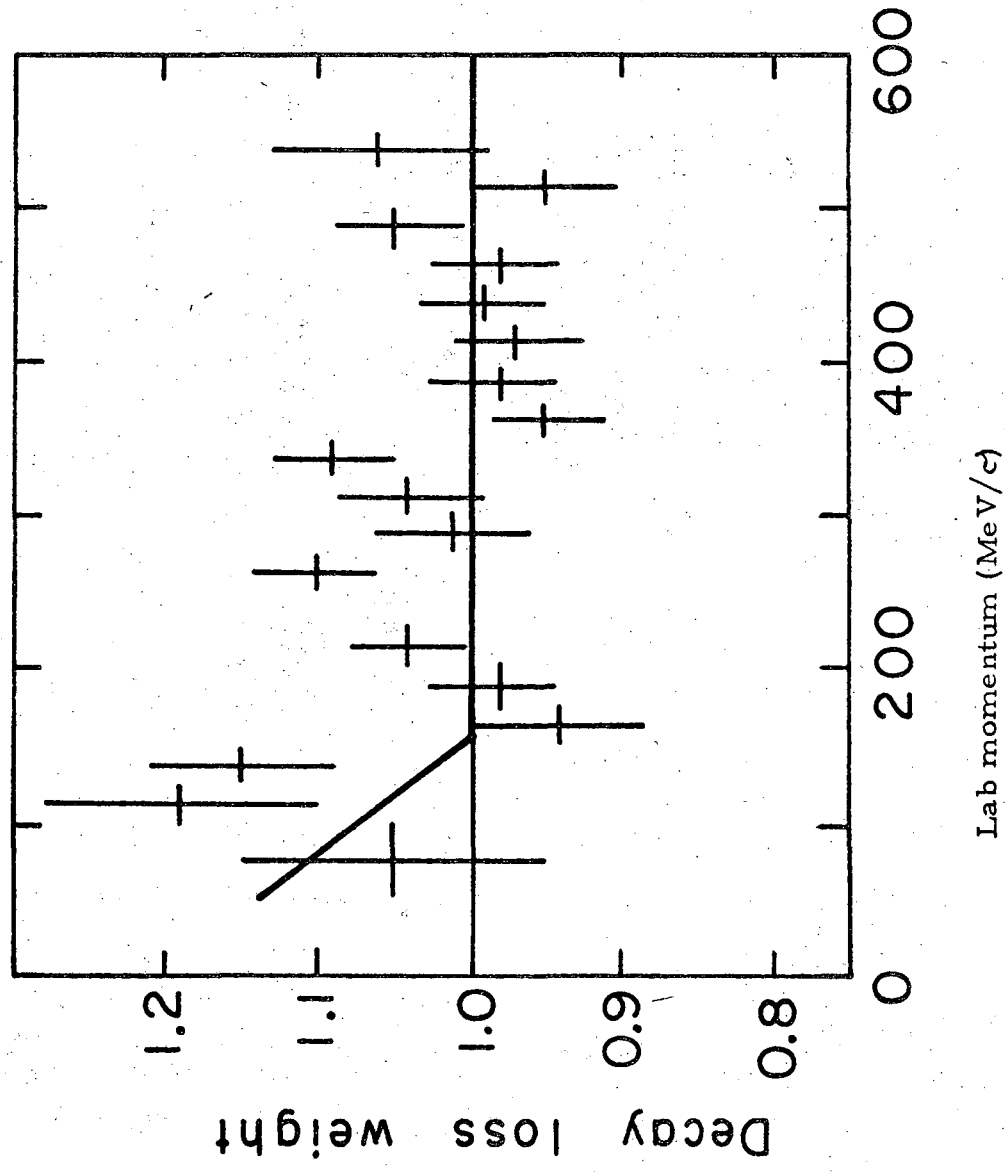
XBL 718 - 4206

Fig. 18



XBL 718-4203

Fig. 19



XBL718 - 4212

Fig. 20

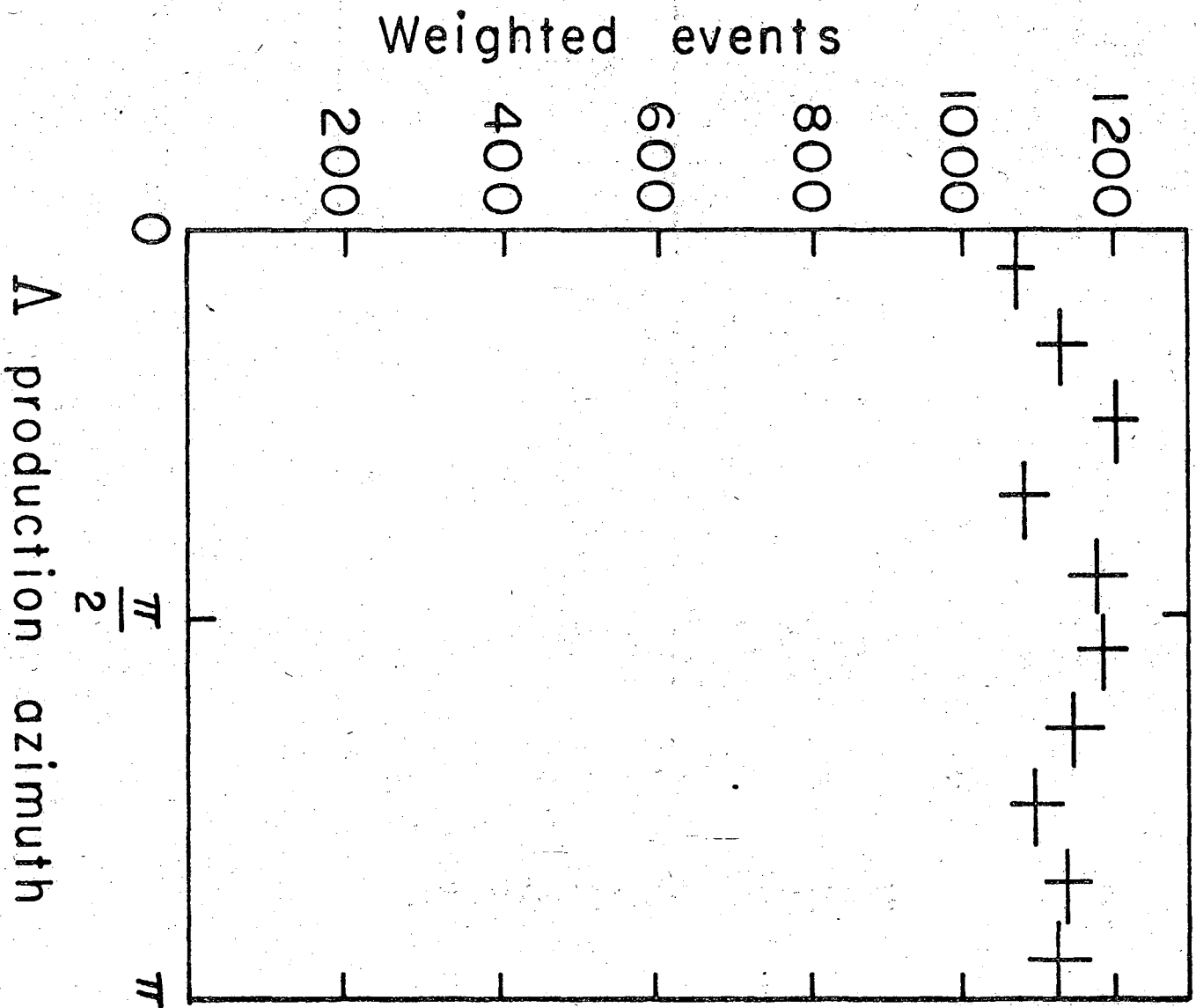
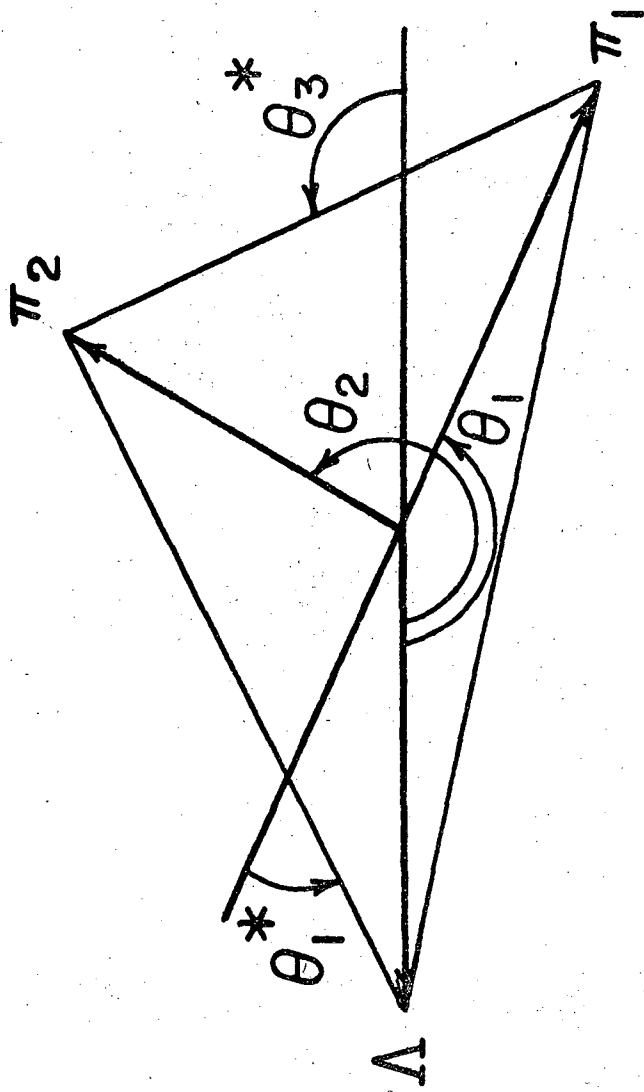


Fig. 21

XBL718-4201



XBL 718-4200

Fig. 22

LEGAL NOTICE

*This report was prepared as an account of work sponsored by the United States Government. Neither the United States nor the United States Atomic Energy Commission, nor any of their employees, nor any of their contractors, subcontractors, or their employees, makes any warranty, express or implied, or assumes any legal liability or responsibility for the accuracy, completeness or usefulness of any information, apparatus, product or process disclosed, or represents that its use would not infringe privately owned rights.*

TECHNICAL INFORMATION DIVISION  
LAWRENCE BERKELEY LABORATORY  
UNIVERSITY OF CALIFORNIA  
BERKELEY, CALIFORNIA 94720